JAN ROGGE

BARIUM OXIDE AS NOVEL BARRIER IN HEUSLER BASED MAGNETIC TUNNEL JUNCTIONS

BIELEFELD UNIVERSITY

This work was done by myself. Text and figures were partly taken from corresponding publications, which originate directly from this work.

(Jan Rogge)

Reviewers:
Prof. Dr. Andreas Hütten
Prof. Dr. Thomas Huser

BIELEFELD UNIVERSITY, DEPARTMENT OF PHYSICS

THIN FILMS AND PHYSICS OF NANOSTRUCTURES

Dissertation

“If it doesn’t fit, use a bigger hammer!”

- loosely translated German movie title -

Contents

Introduction

Spintronics, a combination of the words "spin" and "electronics", uses the electrons' charge like in common electronics and adds their spin as a secondary degree of freedom what permits numerous new applications. In this context magnetic logics and magnetic random access memory (MRAM) are worth to be mentioned.[1] But probably the most prominent example of spintronics in application is the read head in hard disc drives based on the *Giant Magneto resistance (GMR)* effect introduced by IBM in 1997. For the discovery of this effect Peter Grünberg[2] and Albert Fert[3] were awarded the Nobel price in physics in 2007.

Closely related to the GMR effect is the *Tunnel magnetoresistance (TMR)* which was first only measured at 4.2 K and described by Jullière[4] in 1975. The TMR effect occurs in *magnetic tunnel junctions (MTJs)* which basically consist of two ferromagnetic layers separated by a thin insulating layer, the so called tunneling barrier. The resistance of such a device strongly depends on the relative magnetization of the ferromagnets, generally being minimum for parallel (R_p) and maximum for anti-parallel orientation (R_ap). The relative change in resistance defines the TMR ratio: $TMR = \frac{R_\mathrm{ap}-R_\mathrm{p}}{R_\mathrm{p}}$.[5] According to Jullière the TMR can also be expressed in terms of the spin polarizations $P_{1/2}$ of the two ferromagnetic films, which are connected to their spin dependent *density of states (DOS)* at the Fermi energy (E_F), by $TMR = \frac{2P_1P_2}{1-P_1P_2}$. This two current model in which the electrons maintain their spins while tunneling through the barrier layer is visualized in Figure 1. In the case of parallel magnetizations (a) the number of states in both ferromagnets are equal and every tunneling electron from FM1 can occupy a state in FM2 with the correct spin. The measured resistance is small. For anti-parallel aligned magnetizations (b) electrons from the spin channel with the larger number of states only find a small number of free

[1] G. A. Prinz, *Science*, vol. 282, no. 5394, pp. 1660–1663, 1998; S. A. Wolf, D. D. Awschalom, *et al.*, *Science*, vol. 294, no. 5546, pp. 1488–1495, 2001.

[2] J. Barnaś, A. Fuss, *et al.*, *Phys. Rev. B*, vol. 42, pp. 8110–8120, 13 1990.

[3] M. N. Baibich, J. M. Broto, *et al.*, *Physical Review Letters*, vol. 61, pp. 2472–2475, 1988.

[4] M. Jullière, *Physics Letters A*, vol. 54, pp. 225–226, 1975.

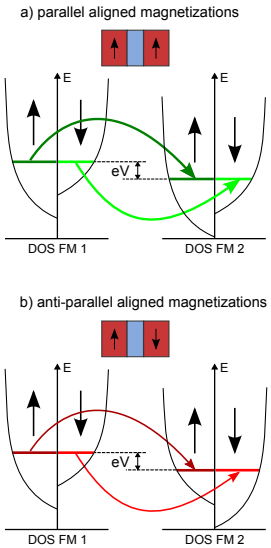

Figure 1: Two current model of the tunneling process for a) parallel aligned magnetizations and b) anti-parallel aligned magnetizations of the two ferromagnets (FM).

[5] This is the optimistic definition of the TMR ratio. Jullière's original definition is $TMR = \frac{R_\mathrm{ap}-R_\mathrm{p}}{R_\mathrm{ap}}$.

states in FM2 and the few electrons with the opposite spin see an excessive number of suitable free states in FM2 which results in a high resistance.

Consequently, materials having a high spin polarization are demanded to enhance the TMR ratio, at best a spin polarization of 100 %. Such materials are called *half-metals* showing metallic behavior for one spin channel and semiconducting or insulating behavior for the other spin direction. For applications a further important requirement is that this property is maintained at temperatures clearly above RT, i.e. materials with a high *Curie temperature* T_c are sought. This applies to some Co based Heusler compounds, which are predicted to be half-metallic,[6] if existing with a certain high ordering, and have a high T_c[7] as well.

Not until 1995 the TMR was realized at room temperature (RT), when Moodera et al.[8] and Miyazaki and Tezuka[9] independently of each other could measure the TMR effect on $CoFe/Al_2O_3/Co$ and $Fe/Al_2O_3/Fe$ MTJs respectively. Meanwhile the RT TMR ratio could strongly be increased from 11.8 % and 18 % respectively to over 600 %[10] by substituting crystalline MgO for the amorphous Al_2O_3 tunneling barrier. The tunneling through the crystalline barrier can no longer be described by Jullière's model, where the tunneling is purely governed by the two electrodes' spin polarizations, but by *coherent tunneling*. Here, the tunneling conductance depends on the symmetry of the Bloch states in the ferromagnetic electrodes and of evanescent states in the barrier.[11] Because Bloch states with different symmetries show different decay rates in the barrier layer, the TMR ratio can greatly be enhanced compared to tunneling through an amorphous barrier.

Therefore this high TMR ratio could be obtained, even though theoretically and experimentally[12] obtained spin polarization of the used electrode material, crystalline fcc CoFeB, is only 41.4 % and 44 %[13] respectively. Very recent studies have indeed found a spin polarization of ~ 65 % for $Co_{0.62}Fe_{0.26}B_{0.12}$ annealed at 300 °C,[14] but this result is still far away from the value of $P = 86.6$ % when applying Jullière's formula.

Hence, combining highly spin polarized electrodes with a lattice matched barrier material – thereby offering the condition for epitaxial crystal growth – should lead to even larger TMR ratios. But this have not been accomplished yet utilizing potentially half-metallic Heusler compound electrodes and a crystalline MgO tunneling barrier, although high TMR values of up to 1995 % at 4.2 K and 330 % at RT have very recently

[6] B. Balke, G. H. Fecher, *et al.*, *Phys. Rev. B*, vol. 74, p. 104 405, 2006; G. H. Fecher and C. Felser, *Journal of Physics D: Applied Physics*, vol. 40, no. 6, p. 1582, 2007.

[7] P. Webster, *Journal of Physics and Chemistry of Solids*, vol. 32, no. 6, pp. 1221 –1231, 1971.

[8] J. S. Moodera, L. R. Kinder, *et al.*, *Phys. Rev. Lett.*, vol. 74, no. 16, pp. 3273–3276, 1995.

[9] T. Miyazaki and N. Tezuka, *Journal of Magnetism and Magnetic Materials*, vol. 139, pp. L231–L234, 1995.

[10] S. Ikeda, J. Hayakawa, *et al.*, *Applied Physics Letters*, vol. 93, no. 8, p. 082 508, 2008.

[11] W. H. Butler, X.-G. Zhang, *et al.*, *Phys. Rev. B*, vol. 63, p. 054 416, 2001.

[12] The spin polarization was measured with superconducting tunneling spectroscopy (STS) by Meservey and Tedrow [MT94].

[13] P. V. Paluskar, J. J. Attema, *et al.*, *Phys. Rev. Lett.*, vol. 100, p. 057 205, 2008.

[14] H. Yang, S.-H. Yang, *et al.*, *AIP Advances*, vol. 2, no. 1, p. 012 150, 2012.

been reported[15] for $Co_2Mn_\alpha Si_\beta$/MgO/$Co_2Mn_\alpha Si_\beta$ MTJs with (co-)sputtered electrodes and e^--beam evaporated MgO barrier. The highest RT TMR employing Heusler electrodes could be achieved with the quaternary Heusler $Co_2FeAl_{0.5}Si_{0.5}$ and MgO barrier completely deposited by *molecular beam epitaxy (MBE)*.[16] In industry, the deposition method of choice is sputtering due to its applicability in large scale productions. On the contrary, MBE offers more control over the growth parameters. We have decided to investigate MTJs with lower Co_2FeSi and Co_2FeAl electrodes fabricated by MBE and sputtering respectively. As the smaller lattice mismatch between Co_2FeSi and BaO compared to Co_2FeSi and MgO offers better conditions for a coherent electrode - barrier interface, BaO was chosen as novel barrier material to experimentally reveal the potential half-metallicity of this Heusler compound. Also the study of Co_2FeAl based MTJs with a BaO barrier promises to yield interesting results due to the comparable but reverse lattice mismatch of these two materials compared to that of Co_2FeAl and MgO.

In this work we have deposited Co_2FeSi layers by different MBE techniques from separate sources and investigated their properties concerning their use as ferromagnetic bottom electrode in MTJs, i.e. magnetic, surface, and structural properties. For the latter aspect it has been of special interest to find appropriate growth parameters to achieve (001) orientated, at least B2 ordered thin films. For the BaO layers, which have been grown by the evaporation of Ba metal in an O_2 atmosphere, the same crystal orientation is demanded to assure epitaxial growth and coherent interfaces, while simultaneously as second requirement concerning the tunneling barrier a sufficient surface smoothness is needed.

Based on these results Co_2FeSi/BaO/Fe MTJs have been prepared and their transport properties both at RT and at low temperatures studied. Furthermore, we have investigated the transport properties of BaO based MTJs with a sputtered Co_2FeAl lower electrode and an Fe top electrode.

[15] H.-X. Liu, Y. Honda, *et al.*, *Applied Physics Letters*, vol. 101, no. 13, p. 132 418, 2012.

[16] N. Tezuka, N. Ikeda, *et al.*, *Applied Physics Letters*, vol. 94, no. 16, p. 162 504, 2009.

Publications and conferences as main author

- J. Rogge, P. Hedwig, C. Sterwerf, A. Hütten: Co_2FeSi based Magnetic Tunnel Junctions with BaO barrier, *IEEE Transactions on Magnetics*, Volume 48, Issue 11, pp. 3825-3828, 2012

- J. Rogge, A. Hütten, *Investigation on Fe/NaCl/Fe Magnetic Tunnel Junctions grown with a Sputtering - Molecular Beam Epitaxy Hybrid Technique*, nanoelectronics days, Aachen (2008), Talk on Wednesday, May 14, 14:30

- J. Rogge, A. Regtmeier, A. Hütten, *Investigation of thermally evaporated Fe/MgO/Fe MTJs and NaCl layers*, DPG spring meeting, Dresden (2009), Poster MA 40.107

- J. Rogge, F. Schmid-Michels, A. Hütten, *Magnetic and structure studies on thin films of (co-)evaporated Heusler compounds*, DPG spring meeting, Regensburg (2010), Poster MA 33.55

- J. Rogge, P. Hedwig, C. Sterwerf and A. Hütten, *Co_2FeSi based Magnetic Tunnel Junctions with BaO barrier*, Intermag, Vancouver (2012), Talk FE-08

Experimental details

This chapter will give a short overview of the employed deposition system and also some information about the e^--beam-lithography process. Due to the properties of BaO a conventional microstructuring holds (predominantly) incalculable influences, so that the strategy of MTJ fabrication has been adjusted several times to minimize these influences.

Deposition system

For the fabrication of all samples a Leybold L560 sputtering system is used which had been extended by an MBE system. The L560 with a base pressure of $\sim 3 \times 10^{-7}$ mbar is connected via the load-lock ($p < 3 \times 10^{-7}$ mbar) with the mainly custom made MBE system that has a base pressure of $\sim 7 \times 10^{-10}$ mbar. A detailed description of all features can be found in my diploma thesis.[17]

Starting in 2009 the deposition system has been further improved. The sputtering unit has been equipped with a RF source which is basically used for the deposition of MgO layers. Furthermore, the operation of the MBE system has been made fundamentally easier by a control program written in LabView. This tool offers the possibility to regulate all Knudsen cells' proportional-integral-derivative (PID) controllers centrally and to operate the deposition processes. Different operation modes are available for the automated deposition of single layer stacks, multilayer stacks, and for co-evaporation from different sources at the same time. Additionally, the rotation and temperature of the sample holder can be controlled. Fabian Schmid-Michels was engaged in the automation of the deposition processes thoroughly in his bachelor thesis.[18]

Moreover, two additional custom made Knudsen cells[19] and an e^--beam evaporator with two sources have been installed. So overall, there are up to 11 materials available for deposition,

[17] J. Rogge, "Untersuchungen an vollständig thermisch gedampften Fe/MgO/Fe Tunnelelementen und NaCl Schichten", Diplomarbeit, Bielefeld University, 2008.

[18] F. Schmid-Michels, "Herstellung und Charakterisierung von Co_2FeMg", Bachelor's Thesis, Bielefeld University, 2010.

[19] A detailed description of the engineered Knudsen cells including sketches can be found in the Appendix.

three DC and one RF magnetron sputtering sources, 5 Knudsen cells, and two e^--beam evaporation sources.

e^--beam lithography

In order to structure the TMR layer stacks e^--beam lithography techniques have been employed. Concretely, the samples were coated with the negative e^--beam resist AR-N 7520.18 from Allresist using a spin coater. The structures were then written employing a *Leo 1530 Scanning electron microscope (SEM)* system with a high precision stage by *Raith GmbH*. The shape of the MTJs was chosen to be elliptical with four different sizes of $(6 \times 2)\ \mu m^2$, $(3 \times 1)\ \mu m^2$, $(1 \times 0.3)\ \mu m^2$ and $(0.6 \times 0.2)\ \mu m^2$ (see the first layer in Figure 2). This shape provides two beneficial properties. On the one hand the magnetic easy axes are along the ellipses' major axes due to shape anisotropy. On the other hand dipole coupling makes sure that the magnetizations of the two magnetic electrodes are predominantly antiparallel aligned without an outer magnetic field.

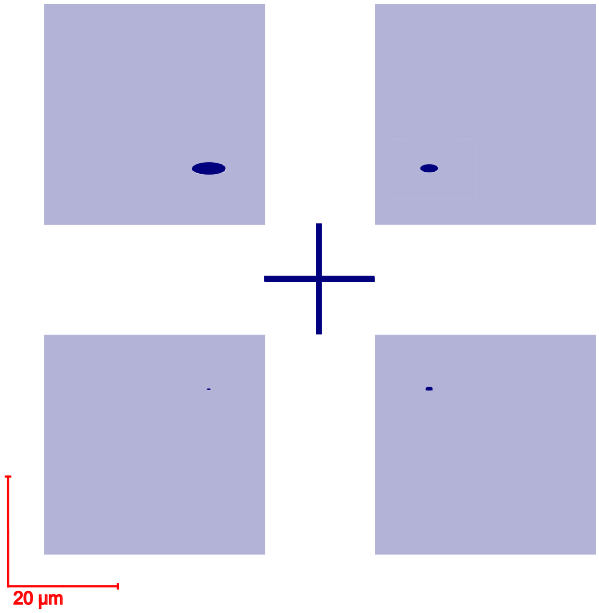

Figure 2: First version of the e^--beam lithography structures. First layer (dark blue): Elliptically shaped MTJs with dimensions (starting in the upper left corner, continuing clockwise) $(6 \times 2)\ \mu m^2$, $(3 \times 1)\ \mu m^2$, $(1 \times 0.3)\ \mu m^2$ and $(0.6 \times 0.2)\ \mu m^2$ and centering cross. Second layer (light blue): Contact pads for the upper electrode.

After writing an array of ellipses and developing the resist the MTJs are carved out by Ar-ion beam etching. The etching system is additionally equipped with a *secondary ion mass spectrometry (SIMS)* system which provides the possibility to see which layer of the sample is momentarily penetrated by the ion beam. Once the approximate middle of the lower electrode is reached the etching process is stopped and the sample transferred into a sputtering machine to fill up the empty space with TaO_x. In this process the time the sample is exposed to the atmosphere has to be minimized in order to protect the sensitive BaO barrier layer from air moisture and O_2 (see section "Barium Oxide" on page 37).

Afterwards, the resist is removed. Basically the MTJs could now be measured directly, but as the surface areas of the MTJs are too small to contact them with a needle probe, contact pads are added to the MTJs. This is realized by sputtering 5 nm Ta[20] and 50 nm Au on top of the samples, coating them with the e^--beam resist and writing the contact pads in the SEM (see the second layer in Figure 2). After developing, the final etching and resist removal the MTJs are finished and ready to be measured. The complete lithography process is shown schematically in Figure 3.

[20] Ta is only used as an adhesive layer as otherwise the Au layer would not stick to the surface.

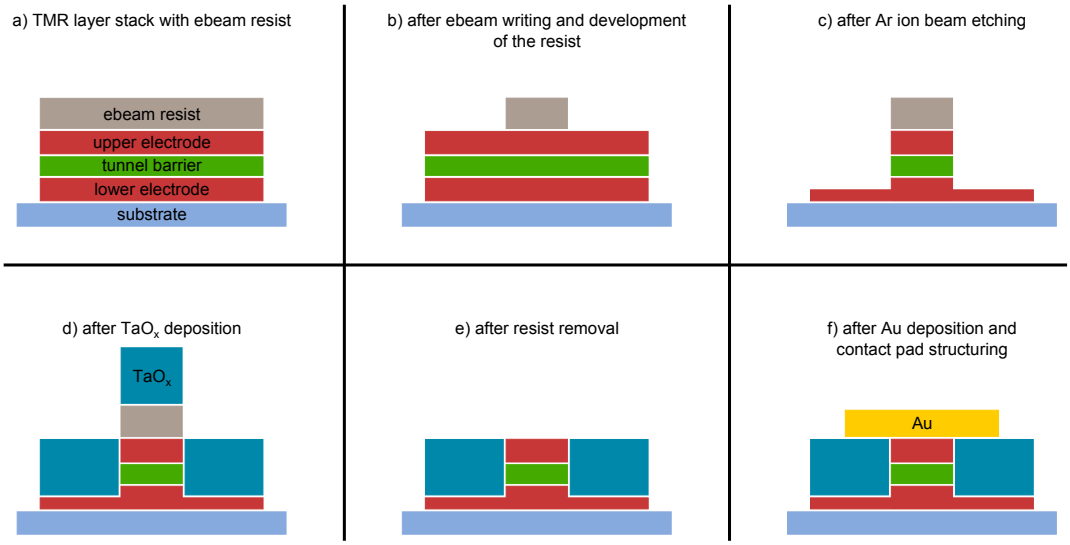

Figure 3: Schematic and idealized illustration of important steps of the lithography process: the sample with the TMR layer stack after a) spin coated with the e^--beam resist, b) writing of the structures and development of the resist, c) Ar ion beam etching, d) deposition of TaO_x, e) removal of the remaining resist, f) deposition of 5 nm Ta + 50 nm Au and another complete lithography cycle for the contact pads.

The described microstructural design turned out to have a weak point. To be specific, the large area of the contact pads which allows to contact the top electrode also increases the possibility of producing a short circuit between a contact pad and the underlying lower electrode at positions where there are small holes or cracks in the TaO_x surface.[21] The lower electrode expanding over the whole sample plane furthermore increases the probability of short circuits caused by bonding the contact pads to a chip carrier which is mandatory for low temperature measurements.

[21] As the remaining resist is very hard after the TaO_x deposition and for the most part covered by the insulator, a heated (60 °C) ultrasonic bath is needed to get the resist off the sample. During this two hour treatment it is likely that also TaO_x sporadicly peels off and a small hole is left behind.

In order to avoid these shorts the microstructural design was modified and further improved. Therefore a third lithography step prior to the already described ones have been introduced. The first lithography layer (see the greenish structures in Figure 4) prepares stripes which finally will build the lower elec-

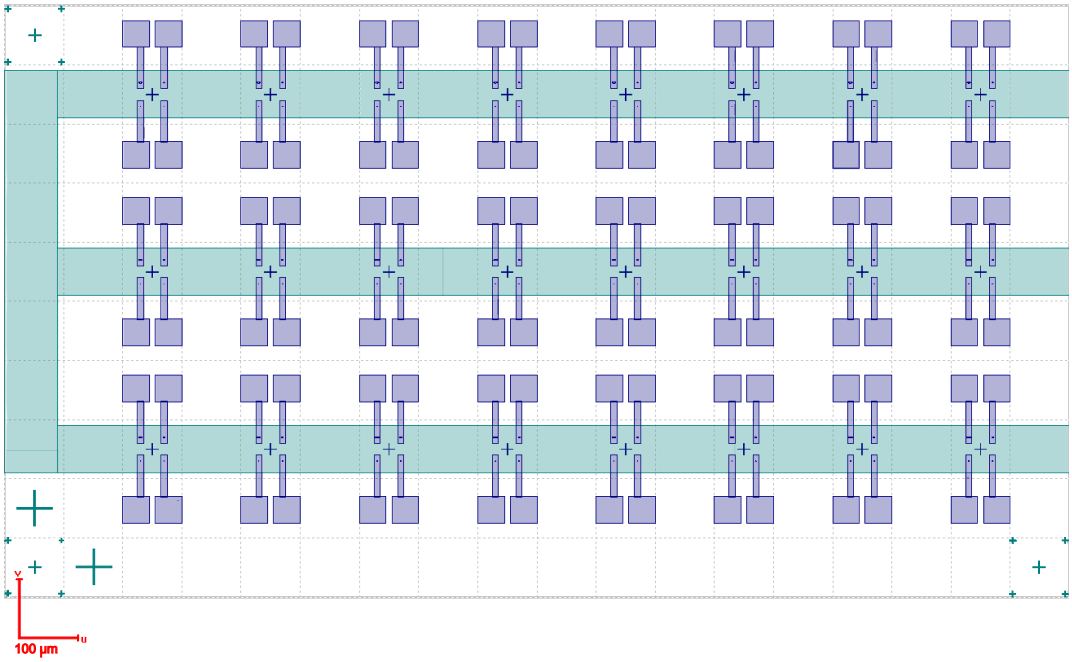

Figure 4: Final version of the produced structures. First layer (green): Orientation marks and conduction stripes for the lower electrodes. Second layer (dark blue): Elliptically shaped MTJs and orientation crosses. Third layer (light blue): conduction lines and pads for the upper electrode.

trode. The first etching step is stopped before the barrier layer is reached, the resist removed and the sample subsequently cov-

ered with resist again. In the second writing cycle the elliptical MTJs are structured on these stripes, whereby the white areas in Figure 4 are milled to the bare substrate during the following etching process. Without breaking the vacuum the sample is then covered with TaO_x using a sputter source which has been additionally installed in the load-lock of the etching machine. In the final lithography cycle the contact pads are then placed on those areas where, despite of the sputtered insulator, only the substrate lies beneath and connected with the upper electrodes of the MTJs by narrow conducting lines (see light blue third layer in Figure 4). Thus the area which could be short circuited with the lower electrode through a hole in the TaO_x layer is minimized. In Figure 5 the SEM picture of a completed sample in the area of the MTJs is shown. The MTJs underneath the conducting lines can clearly be identified and are marked by red ellipses additionally. Compared to the orientation of the scheme in Figure 4 the view is rotated clockwise by about $90\,^\circ$, so that the $(6 \times 2)\ \mu m^2$ MTJs are in the upper right area of the picture (marked with "A"). The aimed dimensions of the MTJs

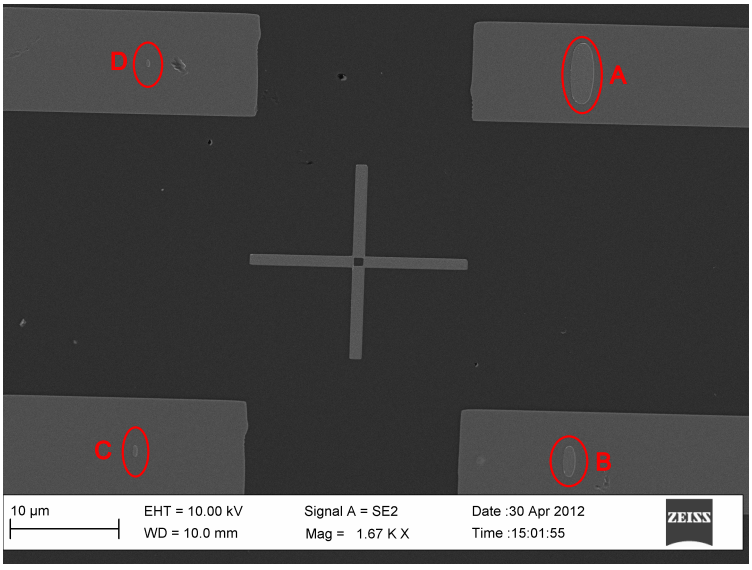

Figure 5: SEM picture of the completed sample in the area of the MTJs with the conducting lines on top. The MTJs are marked with red ellipses and capital letters: A) $(6 \times 2)\ \mu m^2$, B) $(3 \times 1)\ \mu m^2$, C) $(1 \times 0.3)\ \mu m^2$ and D) $(0.6 \times 0.2)\ \mu m^2$

differ slightly from the real ones. As can be seen in Figure 6 the actual sizes are: $(6.226 \times 2.042)\ \mu m^2$ (A), $(3.124 \times 1.033)\ \mu m^2$ (B), $(1.032 \times 0.304)\ \mu m^2$ (C) and $(0.626 \times 0.222)\ \mu m^2$ (D). In the following the nominal dimensions will be used for simplicity,

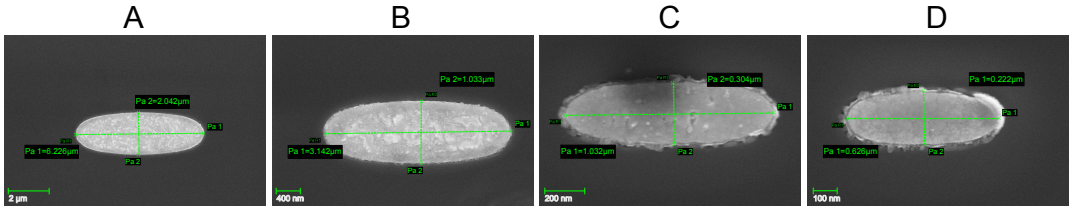

Figure 6: SEM pictures of the MTJs right after the etching process is finished with the actual dimensions. The labels (A - D) are the same as in Figure 5.

but whenever the MTJs' areas are needed for calculations the just given measured values will be applied.

Heusler compounds

In this chapter the history and basics of so called *Heusler alloys* or better *Heusler compounds* will be discussed. Furthermore, the sample preparation will be described and the results of investigations on the fabricated Heusler layers presented. These include *x-ray diffraction (XRD)*, *alternating-gradient magnetometer (AGM)*, *atomic force microscopy (AFM)*, *x-ray absorption spectroscopy (XAS)* and *x-ray magnetic circular dichroism (XMCD)* measurements.

History and basics

The material class of Heusler compounds was first discovered in 1901 by the German chemist and mining engineer *Friedrich Heusler*.[22] He found Cu_2MnSn to be ferromagnetic even though each constituent separately is not.[23] One differentiates between *Full Heuslers* with the chemical notation $\mathbf{X_2YZ}$ and *Half Heuslers* with the formula **XYZ**. **X** and **Y** are transition metal atoms and **Z** denotes a semiconductor or non-magnetic metal atom (compare Figure 7).

The crystal structure plays a crucial role for the magnetic properties of the Heusler compound. The highest ordered Full Heusler configuration is the $L2_1$ *phase*. Here a unit cell consists of 4 interpenetrating fcc sublattices of **X** atoms occupying the sublattices at the positions (0, 0, 0) and (1/2, 1/2, 1/2), with **Y** at (1/4, 1/4, 1/4) and with **Z** at (3/4, 3/4, 3/4) (see Figure 8 a). If there is **Y-Z** disorder, which means those atoms can switch their positions within the lattice, the Heusler compound is in the *B*2 *phase* (see Figure 8 b). Finally if all atoms occupy random positions within the lattice only the *A*2 *phase* is present.

In the case of a Half Heusler compound, the **X** atom positions of the sublattice at (1/2, 1/2, 1/2) are vacant. This type of ordering is the $C1_b$ *phase* (see Figure 8 c).

Many Heusler compounds are of special interest for spintronic applications because of their unique properties. First

[22] *01.02.1866 in Dillenburg; †1947.

[23] F. Heusler, W. Starck, *et al., Verhandlungen der deutschen physikalischen Gesellschaft*, vol. Bd. 5, D. P. G. (1899-1945), Ed., pp. 219–232, 1903.

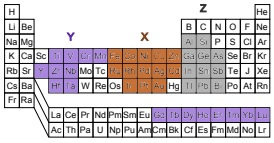

Figure 7: Periodic table with colored areas to indicate which atoms are possible for the X, Y and Z positions.

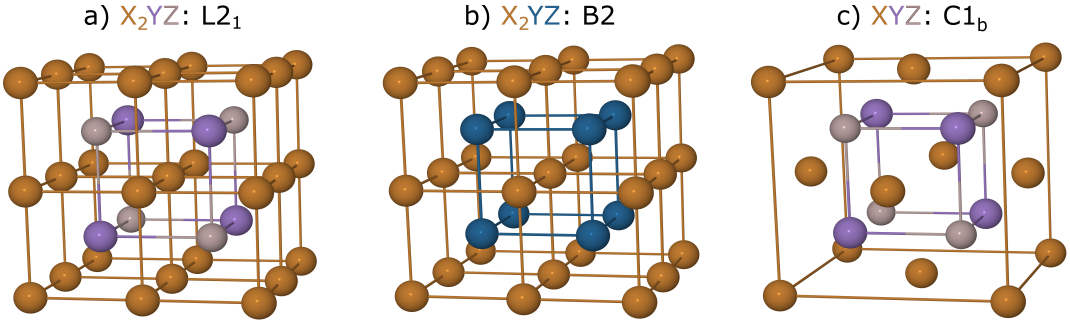

Figure 8: Illustration of the different phases of ordering in the Full Heusler (a: $L2_1$ type and b: B2 type) and Half Heusler lattice (c: $C1_b$). Structures are modeled with *Jmol (Version 13.0.1): http://www.jmol.org/* and rendered with *Persistence of Vision Raytracer (Version 3.6): http://www.povray.org/*

of all their Curie temperatures are usually clearly above room temperature, which makes them applicable in technical applications. Secondly, their low coercivities make Heusler compounds suitable for devices with low energy consumption. And finally many Heusler compounds are predicted to be half metallic, i.e. in the density of states (DOS) these materials' electrons show a metallic behavior at the Fermi energy level (E_F) for one spin channel, while there is a band gap in the other spin channel. This results in 100 % spin polarization and would lead to infinitely high TMR ratios when employing such a Heusler layer as magnetic electrode in an MTJ.[24] For comparison, the regular transition metal ferromagnets Fe, Co and Ni exhibit spin polarizations of only 45 %, 34 % and 11 %. These experimentally obtained values by Tedrow and Meservey [25] are within one percentage point in good agreement with theoretical predictions.[26]

Simulations by Balke et al.[27] and Fecher and Felser[28] predict Co_2FeSi and Co_2FeAl respectively to be half metals. But in the latter case E_F is so close to the edge of the valence band that the half metallicity is very unstable and not expected to be observed at temperatures above 0 K. Fecher furthermore predicts that by substituting half of the Al atoms by Si atoms ($Co_2FeAl_{0.5}Si_{0.5}$) E_F can be moved into the middle of the band gap and thereby stabilizing the Heusler compound's half metallicity. Similarly, one can move E_F away from the conduction band by replacing half of the Fe atoms in Co_2FeSi with Mn atoms ($Co_2Fe_{0.5}Mn_{0.5}Si$) according to Balke. But not only the Heusler compound's composition influences the spin polarization. The structural ordering seems to play the most important role here. B2 ordering instead of $L2_1$[29] or tetragonal distortion[30] for example lead to a significant reduction of the spin polarization. Another important

[24] R. A. de Groot, F. M. Mueller, *et al.*, *Phys. Rev. Lett.*, vol. 50, pp. 2024–2027, 25 1983.

[25] P. Tedrow and R Meservey, *Physical Review B*, vol. 7, no. 1, pp. 318–326, 1973.

[26] M. B. Stearns, *Journal of Magnetism and Magnetic Materials*, vol. 5, pp. 167–171, 1977.

[27] B. Balke, G. H. Fecher, *et al.*, *Phys. Rev. B*, vol. 74, p. 104 405, 2006.

[28] G. H. Fecher and C. Felser, *Journal of Physics D: Applied Physics*, vol. 40, no. 6, p. 1582, 2007.

[29] P. Bruski, S. Erwin, *et al.*, *Physical Review B*, vol. 83, no. 14, pp. 2–5, 2011.

[30] M. Nobori, T. Nakano, *et al.*, *Physical Review B*, vol. 83, no. 10, pp. 1–6, 2011.

factor is the interface. Yu and Yang report on a reduced spin polarization due to charge-discontinuity at the interface between the Heusler compound and the adjacent material which gives rise to interface states.[31] Nevertheless, the two aforementioned Heusler compounds have been studied and integrated into MTJs in the course of this work. Co_2FeSi has been fabricated by MBE methods, while Co_2FeAl layers have been deposited by magnetron sputtering. These two compounds were chosen, because sputtered Co_2FeAl tends to form crystalline layers already at RT and the components of Co_2FeSi can easily be evaporated using Knudsen cells, which our MBE system is equipped with. For the Co_2FeSi layers the primary aim was to obtain an at least B2 structured Heusler film at all as the MBE system in Bielefeld has just been set up. MBE techniques offer the opportunity to easily adjust the stoichiometry of the produced films and thereby to tune their magnetic and electronic properties. Particularly a possible increase of the spin polarization by shifting E_F more towards the middle of the bandgap, would be a huge advantage in terms of improving TMR amplitude.

Beside some Heusler compounds, there are also other predicted half-metals. The most-known among them are Magnetite (Fe_3O_4),[32] CrO,[33] $La_{0.7}Sr_{0.3}MnO_3$ (LSMO),[34] and CrAs.[35] But many of these materials are not suitable for applications due to low Curie temperatures (CrO_2, LSMO). For Fe_3O_4 based MTJs only low TMR ratios are predicted and experimentally obtained because of antiphase boundaries with antiferromagnetic correlations.[36]

Heusler sample preparation

MgO substrates with (001) crystal orientation are used for all Heusler layers. MgO features a cubic crystal structure with a lattice constant of $a_{MgO} = 4.21\,\text{Å}$. When the Heusler layer is deposited on an MgO (001) surface its lattice will preferentially grow rotated by 45 °, so that the effective lattice constant the Heusler layer senses is $a_{MgO,45^\circ} = \sqrt{2} \cdot 4.21\,\text{Å} = 5.95\,\text{Å}$. This means a lattice mismatch of 4.9 % and 3.7 % for Co_2FeSi and Co_2FeAl respectively with regard to the 45 ° rotated MgO (001) lattice.

The first step of the sample preparation process is the deposition of a 5 nm thick MgO buffer layer in order to cover contaminations on the substrate and get a clean surface. This buffer layer is produced by RF magnetron sputtering. The choice

[31] H. L. Yu and G. W. Yang, *Applied Physics Letters*, vol. 98, no. 1, p. 011 910, 2011.

[32] Y. S. Dedkov, U. Rüdiger, *et al.*, *Phys. Rev. B*, vol. 65, p. 064 417, 6 2002.

[33] K Schwarz, *Journal of Physics F: Metal Physics*, vol. 16, no. 9, p. L211, 1986.

[34] J.-H. Park, E. Vescovo, *et al.*, *Nature*, vol. 392, no. 6678, pp. 794–796, 1998.

[35] H. Akinaga, T. Manago, *et al.*, *Japanese Journal of Applied Physics*, vol. 39, p. 1118, 2000.

[36] J. De Teresa, A. Fernández-Pacheco, *et al.*, *Microelectronic engineering*, vol. 84, no. 5, pp. 1660–1664, 2007.

of using MgO (001) substrates with a 5 nm MgO buffer layer is based on the results of D. Ebke who found this combination to yield the best results concerning crystallinity for the used Heusler compounds.[37]

[37] D. Ebke, "Cobalt based Heusler compounds in magnetic tunnel junctions", PhD thesis, Bielefeld University, 2010.

In case of Co_2FeSi the substrate is directly transferred into the MBE chamber, where the Heusler layer is grown by two different MBE techniques.
The first one is the co-deposition from three sources at the same time onto the heated substrate and subsequent in-situ annealing. Those samples will be referred to as *CFS-co*.
The second one is a multilayer method. Here ultra-thin Co, Fe and Si layers are deposited separately and repeatedly onto the substrate and in-situ annealed afterwards. Those samples will be referred to as *CFS-MLM*.

To find the correct stoichiometry in both cases we start with the definition of the *atom rate* r_A in the following way:

$$r_A \equiv \frac{N_A}{t} = \frac{\rho \cdot A \cdot d}{t \cdot m_A} = \frac{\rho}{m_A} \cdot r_d \cdot A$$

with N_A the total number of atoms, t the evaporation time, ρ the density of the evaporated material, A the area of the film, d the film thickness, m_A the atomic weight of the actual material and $r_d = {}^{d}/_{t}$ the evaporation rate (in terms of layer thickness per time). Now the weighting factor f can be defined as

$$f \equiv \frac{\rho}{m_A}$$

to be able to choose the correct evaporation rates and layer thicknesses according to the aimed atomic ratio of the Heusler layer.

For the CFS-co samples we can set up individual terms for the atom rates of Co ($r_{A,\,Co}$), Fe ($r_{A,\,Fe}$) and Si ($r_{A,\,Si}$). Considering the identical sample areas the simplest expressions are:

$$r_{A,\,Co} \sim f_{Co} \cdot r_{d,\,Co} \quad ; \quad r_{A,\,Fe} \sim f_{Fe} \cdot r_{d,\,Fe} \quad \text{and} \quad r_{A,\,Si} \sim f_{Si} \cdot r_{d,\,Si} \,.$$

For Co_2FeSi the number of Co atoms is twice the number of Fe and Si atoms, hence:

$$r_{A,\,Co} = 2 \cdot r_{A,\,Fe} \quad \text{and} \quad r_{A,\,Co} = 2 \cdot r_{A,\,Si} \,.$$

If we now choose $r_{d,Co}$ to be fixed, the evaporation rates of Fe and Si can easily be calculated by

$$r_{d,\,Fe} = \frac{f_{Co}}{2 \cdot f_{Fe}} \cdot r_{d,\,Co} \quad \text{and} \quad r_{d,\,Si} = \frac{f_{Co}}{2 \cdot f_{Si}} \cdot r_{d,\,Co}$$

respectively.

For the CFS-MLM samples the detailed multilayer system looks like this:

$$\left[\mathrm{Co}_{0.15\,\mathrm{nm}}|\mathrm{Fe}_{f_{\mathrm{Fe}}/f_{\mathrm{Co}}\cdot 0.15\,\mathrm{nm}}|\mathrm{Co}_{0.15\,\mathrm{nm}}|\mathrm{Si}_{f_{\mathrm{Si}}/f_{\mathrm{Co}}\cdot 0.15\,\mathrm{nm}}\right] \times 50\ .$$

A Co layer thickness of 0.15 nm, roughly 1/4 of the Co_2FeSi lattice constant, has been chosen as basis, so that the thicknesses of the Fe and Si layers can be adjusted using the appropriate weighting factors f. After the deposition of the multilayers onto the moderately heated substrate ($T_{\mathrm{sub}} = 300\,^{\circ}\mathrm{C}$) the sample is in-situ annealed at different temperatures for 1 h.

Finally, for all samples a 3 nm thick MgO protection layer is deposited by RF magnetron sputtering so that the complete layer stack looks like shown in Figure 9.

In the Co_2FeAl case the Co_2FeAl layer is simply deposited on top of the MgO buffer layer by DC sputtering followed by the MgO protection layer. Afterwards the sample is annealed at 500 °C in accordance with the results of Ebke et al.[38] to achieve a highly ordered B2 type crystallization.

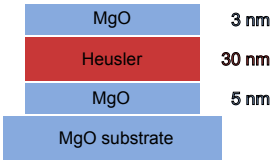

Figure 9: schematic layer arrangement of the Heusler samples.

[38] D. Ebke, P. Thomas, *et al.*, *Journal of Magnetism and Magnetic Materials*, vol. 322, no. 8, pp. 996 –998, 2010.

X-Ray Diffraction Analysis

XRD analysis is employed to determine the crystal structure of the deposited Heusler thin films. A narrow monochromatic x-ray beam hits the sample under an angle θ to the sample's surface normal and is diffracted under the diffraction angle θ according to *Bragg's law*[39] :

$$\lambda = 2d \sin\theta \tag{1}$$

[39] B. Cullity and S. Stock, *Elements of X-ray Diffraction*. Prentice hall Upper Saddle River, NJ, 2001, vol. 3.

with λ being the wavelength of the x-rays and d the lattice spacing in the sample. If the studied sample contains material with a cubic lattice, d can be expressed in terms of the lattice constant a and *Miller's indices* h, k, l as resulting in

$$\sin\theta_{hkl} = \frac{\lambda}{2a}\sqrt{h^2+k^2+l^2}\ . \tag{2}$$

To be able to draw a conclusion about the Heusler layer's crystal structure, one has to have a look at which reflections (hkl) are present in the measured XRD spectrum and which are absent. Webster[40] generally differentiates between three types of x-ray diffractions in case of a Full Heusler with 4 interpenetrating

[40] P. Webster, *Journal of Physics and Chemistry of Solids*, vol. 32, no. 6, pp. 1221 –1231, 1971.

fcc sublattices. In the most unordered case of only A2 type, i.e. all atoms can randomly switch their positions within the lattice, only those x-ray reflections with $(h+k+l)/2 = 2n$ can be observed $(n = 1, 2, 3, \dots)$. Those peaks are *fundamental peaks*.

If B2 ordering is present, i.e. the Co atoms occupy the correct positions within their sublattices and the other two types of atoms are randomly distributed within the other sublattices, peaks with $h+k+l = 2(2n-1)(n = 1, 2, 3...)$ accrue.

For perfect $L2_1$ ordered Heusler compound layers additional reflections arise where all h, k, l are odd (e.g. (111), (311), (333), ...).

Results

The first challenge is to prepare a highly ordered Heusler layer. The crystal structure is investigated by XRD measurements in $\theta - 2\theta$ geometry. Here, the two important reflections in case of (001) orientated layers are the (002) and (004) Heusler peaks. If there is a (004) peak but no (002) reflection, the layer's crystal structure is only A2 ordered, as the (004) peak is a fundamental reflection which is independent of chemical disorder. If both reflections are visible, the Heusler film is at least B2 ordered. The $L2_1$ ordering could further be investigated by XRD measurements using an *Euler cradle*, but these measurements are very time consuming and have not been carried out in the course of this work.

Figure 10 and Figure 11 show the XRD spectra of 30 nm thick Co_2FeSi layers fabricated by co-evaporation and the MBE multilayer method respectively.

For the CFS-co samples the (004) peak is already visible at an annealing temperatures of $T_a = 500\,^\circ\mathrm{C}$. With increasing annealing temperatures its intensity grows and the peak position shifts to higher angles which corresponds to a slight reduction of the out-of-plane lattice constant from 5.68 Å to 5.66 Å. Starting at $T_a = 850\,^\circ\mathrm{C}$ the (002) peak emerges and shows the highest intensity at $T_a = 950\,^\circ\mathrm{C}$. Simultaneously the (004) peak intensity is lowered a bit (see Figure 12) which indicates a higher degree of B2 type ordering.

The CFS-MLM samples show similar characteristics except that the (004) reflection is only a hint of a peak for $T_a < 850\,^\circ\mathrm{C}$. At $T_a = 850\,^\circ\mathrm{C}$ a distinct (004) peak arises along with the (002) reflection. Just as for the CFS-co samples at $T_a = 950\,^\circ\mathrm{C}$ the (002) peak shows the highest intensity and also the (004) peak

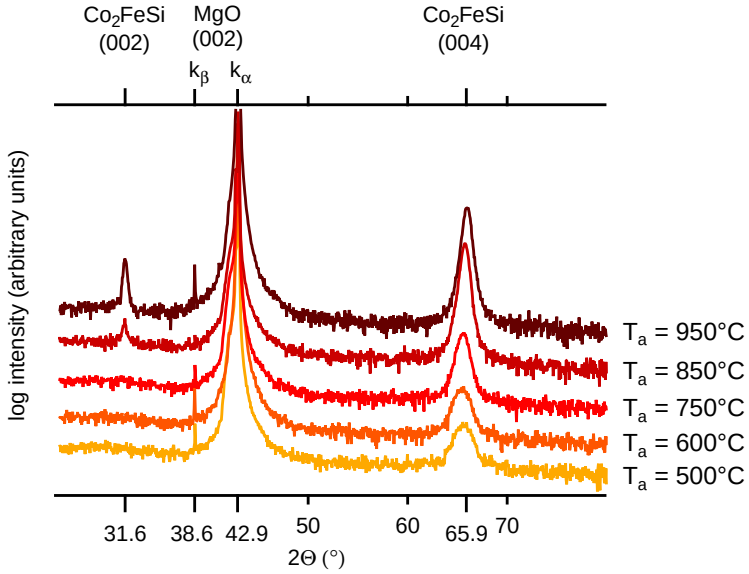

Figure 10: XRD spectra of 30 nm thick Co_2FeSi layers on MgO (001) substrate fabricated by co-evaporation and in-situ post annealed at different temperature T_a for 1 h.

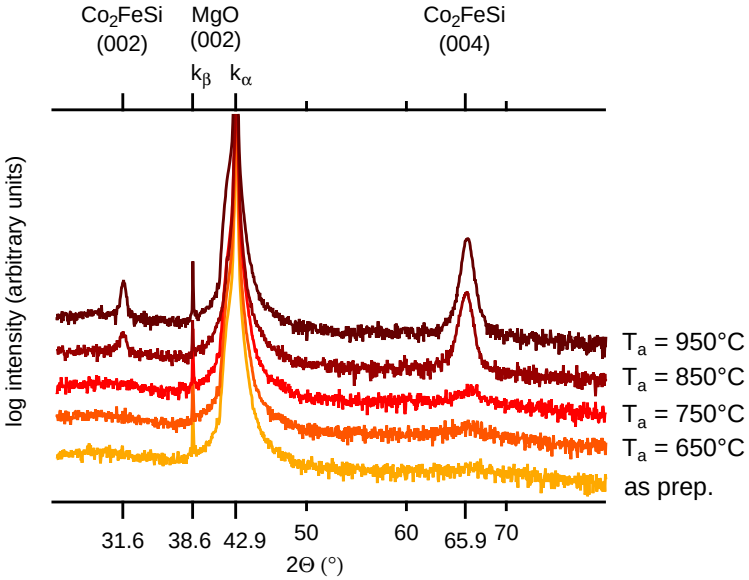

Figure 11: XRD spectra of 30 nm thick Co_2FeSi layers on MgO (001) substrate fabricated by MBE multilayer method and in-situ post annealed at different temperature T_a for 1 h. The curve denoted with 'as prep.' corresponds to a as prepared sample without any annealing.

position is slightly shifted to higher angles. This angular shift coincides with a minor decrease in the out-of-plain lattice constant from 5.66 Å to 5.65 Å. This reduction of the out-of-plain lattice constant means a slight stretching of the in-plane lattice being in agreement with the larger lattice constant of the underlying MgO buffer layer.

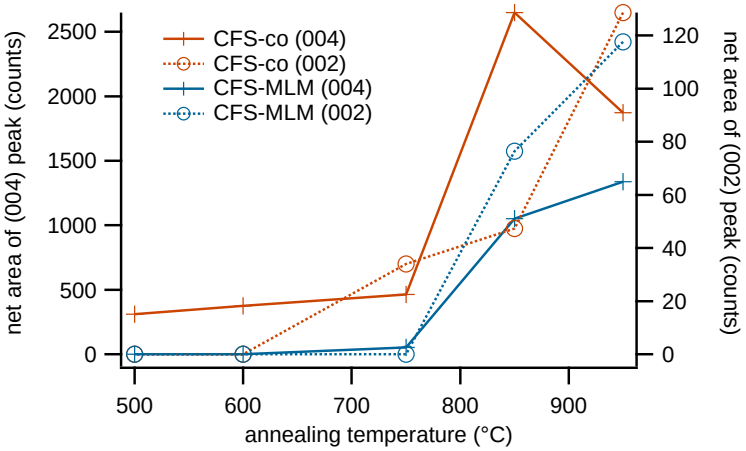

Figure 12: (004) net peak areas (crosses) and (002) net peak areas (circles) of CFS-co (red) and CFS-MLM (blue) samples.

So for both preparation methods an annealing temperature of 950 °C turns out to deliver layers of highest crystallinity. Higher temperatures might result in a higher degree of crystal ordering, but 950 °C is the maximum our experimental setup can reach. To compare both fabrication methods among each other, the ratio of both net peak areas I_{002} and I_{004} are of special interest. As the (002) reflection can only be observed if the investigated sample shows B2 ordering (see section "X-Ray Diffraction Analysis" on page 23) by comparing it with the fundamental (004) peak one obtains a measure for the amount of B2 ordering. Comparing this ratio again with the one obtained from theoretical calculations for a perfectly ordered Heusler sample one gets a quantitative expression for the degree of B2 ordering, S_{B2}[41] :

$$S_{B2} = \sqrt{\frac{I_{002}^{meas} / I_{004}^{meas}}{I_{002}^{calc} / I_{004}^{calc}}} \tag{3}$$

with I_{002}^{meas} and I_{004}^{meas} being the measured peak intensity areas of the (002) and (004) peak respectively while I_{002}^{calc} and I_{004}^{calc} are the corresponding calculated peak intensity areas. Equation 3

[41] P. Webster, *Journal of Physics and Chemistry of Solids*, vol. 32, no. 6, pp. 1221 –1231, 1971; Y. Takamura, R. Nakane, *et al.*, *Journal of Applied Physics*, vol. 105, no. 7, 07B109, 2009.

yields $S_{B2,co} = 84.0\,\%$ for CFS-co and $S_{B2,MLM} = 95.0\,\%$. These two values are quite high. For comparison, the Co_2FeAl layers annealed at 500 °C only exhibit a degree of B2 ordering of 67.8 %.

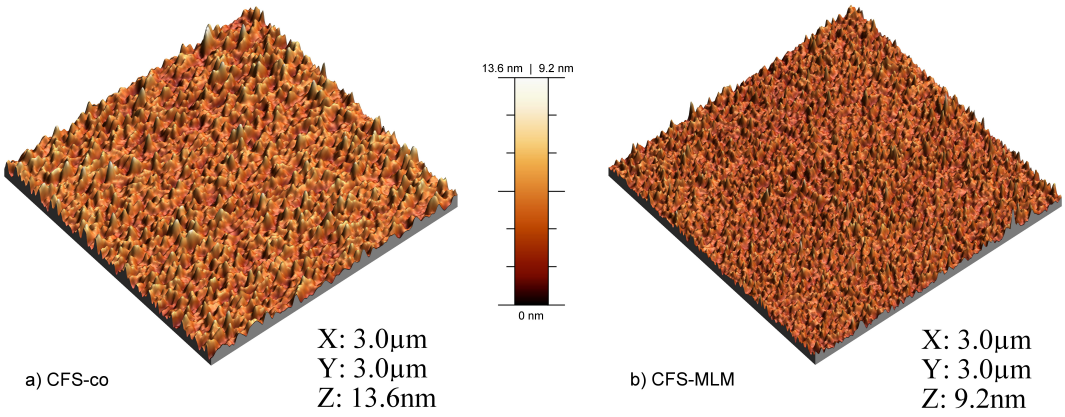

Figure 13: 3D illustration of the surface of a) a CFS-co sample annealed at 850 °C and b) a CFS-MLM sample annealed at 850 °C obtained from AFM measurements in contact mode.

Another important requirement that a potential lower magnetic electrode has to meet is a low surface roughness. If the layer is too rough the barrier layer quality strongly suffers. In particular the probability of pinholes is increased. Besides the higher grade of crystal ordering the CFS-MLM sample surface exhibits a lower roughness with 0.75 nm than the CFS-co sample with 1.52 nm[42] (see fig. 13). This higher smoothness lets the MBE multilayer method appear to be the more suitable technique to grow the lower Heusler electrode.

The Co_2FeAl sample shows an even smaller surface roughness with only 0.205 nm (see Figure 14). The Co_2FeAl layer thickness is reduced to 20 nm according to the film thickness in the MTJs.

The coercivities and magnetic moments per formula unit (f.u.) m were obtained from *alternating gradient magnetometer (AGM)* measurements at RT carried out on a MicroMag 2900 by Princeton Measurement Corporation.[43] Here, the sample of about 3 mm × 3 mm in size is placed on a sample holder attached to a piezo crystal which is positioned between the pole caps of a solenoid. The variable or static DC field of the solenoid is additionally overlaid with an alternating gradient field produced by two coils exerting an alternating force on the sample. This force is proportional to both the magnetic moment of the sample and the magnitude of the gradient field and is sensed by the piezoelectronics. Comparing the results to a calibration mea-

[42] Here the root mean square (RMS) roughness is specified which is expressed as $R_{RMS} = \sqrt{\frac{\sum Z_i^2}{N}}$ with Z_i being the height deviations from the mean image data plane.

[43] *Princeton measurement corporation - micromag 2900 agm magnetometer instruction manual*, 2004.

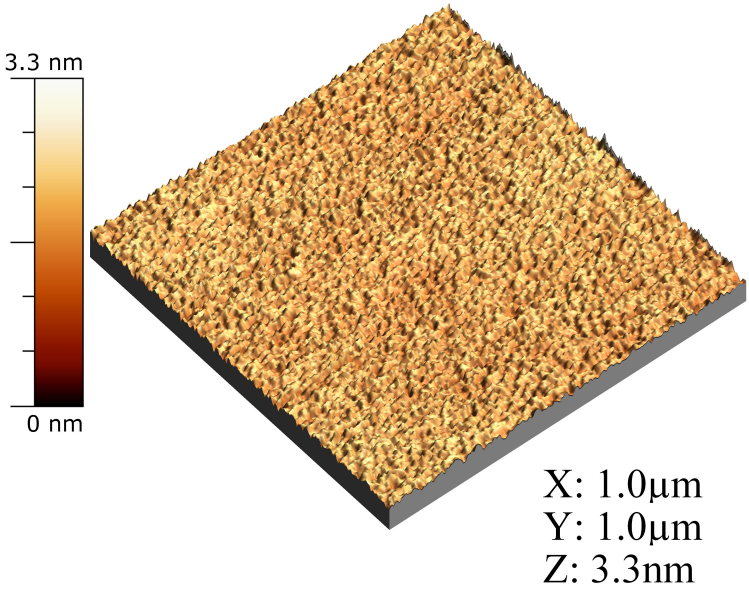

Figure 14: 3D illustration of the surface of a Co_2FeAl sample obtained from AFM measurements. The Co_2FeAl layer thickness is 20 nm.

surement on a sample with known magnetization the sample's overall magnetization M can be obtained. Finally, m is calculated by $m = \frac{M}{V}$ where the magnetic volume V is determined by the sample area[44] and the thickness of the magnetic film.

The AGM measurements show (see Figure 15) a slight increase of the coercive field H_c from $\sim$ 3 Oe to $\sim$ 25 Oe and from $\sim$ 5 Oe to $\sim$ 20 Oe at annealing temperatures T_a of 850 °C and 950 °C for CFS-co and CFS-MLM respectively. These T_a correspond to the temperatures needed for B2 type ordering of the Co_2FeSi films. Gaier et al.[45] observe an increase of H_c with rising T_a on their Co_2MnSi films until the degree of $L2_1$ ordering exceeds a certain value and H_c simultaneously drops again. A similar behavior of H_c with T_a is reported by Oogane et al.[46] on their sputtered Co_2FeAl layers. Both groups call the diffusion of Cr from the buffer layer into the Heusler layer to account for an increased number of magnetic pinning centers and hence the elevated H_c of the Heusler thin films. As the samples investigated in the course of this work do not contain Cr as buffer but MgO which is thermally very stable, this explanation does not apply here. Though Ishikawa et al.[47] also observe an increase of H_c at elevated annealing temperatures on their Co_2MnGe films on MgO substrate with MgO buffer

[44] To obtain the area the sample's weight is measured. Then, by neglecting the mass of the magnetic film, from the substrate density and thickness one gets the sample area.

[45] O. Gaier, J. Hamrle, *et al.*, *Journal of Applied Physics*, vol. 103, p. 103 910, 2008.

[46] M. Oogane, R. Yilgin, *et al.*, *Journal of Applied Physics*, vol. 101, 09J501, 2007.

[47] T. Ishikawa, T. Marukame, *et al.*, *Journal of Applied Physics*, vol. 99, 08J110, 2006.

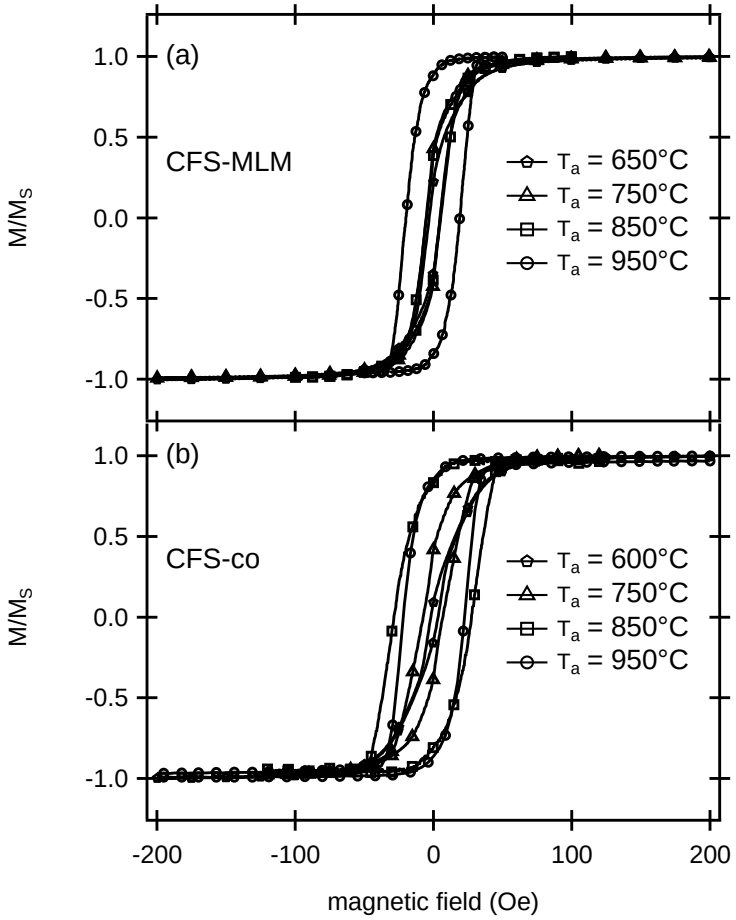

Figure 15: Normalized AGM measurements on a) CFS-MLM samples and b) CFS-co samples annealed at different annealing temperatures T_a.

layer, they do not give any explanation. One approach to interpret this effect is the dependence of H_c on the crystallite size within the film. If the film consists of many, very small crystal grains – which means a lot of tiny single magnetic domains – the magnetization is changed by spin rotation. For small enough crystallites the required energy for the spin rotations is lowered by thermal effects resulting in a small H_c. With increasing grain size the thermal contribution to the spin flip decreases and H_c increases until a certain material dependent critical crystallite diameter is reached. If the crystal grain size increases further the crystallites are not single domain anymore and the magnetization reversal process is no longer governed by spin rotation but domain wall motion. As the latter type of magnetization

change needs less energy than spin flip H_c decreases again.[48] This reasoning could explain the results of Gaier et al. and the obtained T_a dependence of H_c (see Figure 15) on our samples.

From the XRD spectra (see Figure 10 and Figure 11) the integral width B of the characteristic Heusler reflections can be extracted to calculate the mean crystallite diameter L perpendicular to the reflecting lattice plane using the *Scherrer equation*[49] modified by the factor C_{IB}[50] which accounts for the angular dependent instrumental broadening of the peak:

$$L = \frac{K \cdot \lambda}{\sqrt{B^2 - C_{IB}^2} \cos\theta} \tag{4}$$

with K being the shape factor[51] and λ the wavelength of the irradiated x-rays. As the Cu $K_{\alpha 1}$ emission line is used $\lambda = 1.5405980\,\text{Å}$ applies. Executing Equation 4 gives the correct

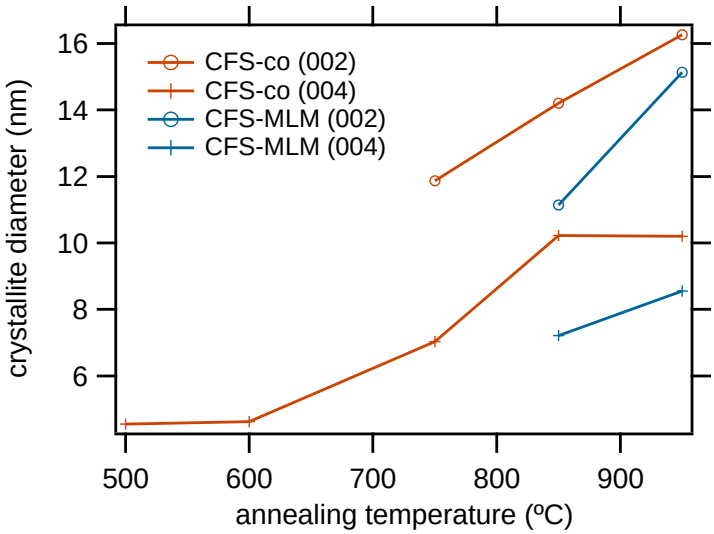

Figure 16: Crystallite diameter as a function of annealing temperature calculated using Equation 4 for CFS-co and CFS-MLM (002) and (004) XRD reflection respectively. The grain sizes obtained from (004) peaks are smaller due to strain effects whose contribution grows with increasing reflection angles.

tendency of growing crystallite size with increasing temperature (see Figure 16), but using the integral widths of the (002) peaks systematically results in larger crystal diameters compared to the (004) peak data. This discrepancy is due to another contribution to the peak broadening caused by strain effects. The Williamson-Hall analysis[52] accounts for this influence, but reliable results require three orders of the same reflection (here the (006) peak

[48] S. H. Liou, S Malhotra, *et al.*, *Journal of Applied Physics*, vol. 70, p. 5882, 1991.

[49] P. Scherrer, *Göttinger Nachrichten*, 1918; R. Zsigmondy and P. Scherrer, *Kolloidchemie: ein Lehrbuch*, ser. Chemische Technologie in Einzeldarstellungen. O. Spamer, 1920.

[50] The correction term for the (002) peak is 0.18° and for the (004) peak 0.25°

[51] K is ~ 0.9 for cubic lattices.

[52] G. Williamson and W. Hall, *Acta Metallurgica*, vol. 1, no. 1, pp. 22–31, 1953.

would be needed in addition to the (002) and (004) peaks) and it would not change the observed tendency of growing crystallite size with increasing annealing temperature. On this account, a further analysis is set aside at this point.

With the largest obtained grain size of $\sim 16\,\mathrm{nm}$ the maximum diameter of 30 nm which corresponds to the layer thickness could not be reached. Nevertheless, considering the acquired grain diameters the crystallite size dependence of H_c is consistent with the AGM findings and confirms the predominant B2 instead of $L2_1$ type ordering of the investigated Co_2FeSi layers.

The absence of $L2_1$ ordering is also the reason for the decreased magnetic moment. In Figure 17 the magnetic moment per formula unit at RT is shown in dependence of the annealing temperature T_a for CFS-co (a) and CFS-MLM (b) samples. The

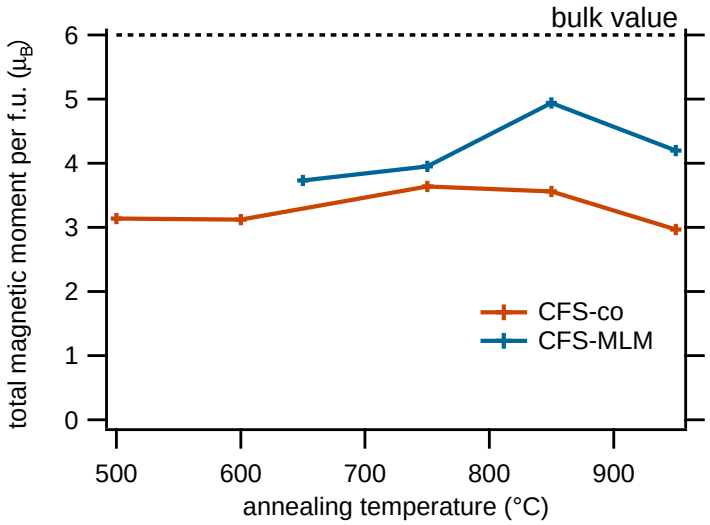

Figure 17: Magnetic moment per formula unit at RT as a function of the annealing temperature T_a for a) CFS-co and b) CFS-MLM samples. Results are obtained from AGM measurements at RT.

magnetic moment increases with rising T_a until a maximum at $T_a = 750\,^\circ\mathrm{C}$ and $T_a = 850\,^\circ\mathrm{C}$ for CFS-co and CFS-MLM respectively. The CFS-MLM samples generally exhibit a higher magnetic moment with a maximum value of $4.94\,\mu_B$ which is still far away from the theoretical values between $5.27\,\mu_B$[53] and $6\,\mu_B$.[54] Also experimental results yield a magnetic moment of $6\,\mu_B$ per formula unit.[55] All the aforementioned data apply to the magnetic moment at 0 K.

There was the possibility to carry out *X-ray Absorption Spec-*

[53] I. Galanakis, P. Dederichs, *et al.*, *Physical Review B*, vol. 66, no. 17, pp. 1–9, 2002.

[54] S. Wurmehl, G. Fecher, *et al.*, *Physical Review B*, vol. 72, no. 18, pp. 1–9, 2005.

[55] S. Wurmehl, G. H. Fecher, *et al.*, *Applied Physics Letters*, vol. 88, no. 3, p. 032 503, 2006.

troscopy (XAS) and *X-Ray Magnetic Circular Dichroism (XMCD)* measurements on two selected specimens. Hence, a CFS-MLM and a Co_2FeAl sample have been chosen. Both samples were deposited on MgO (001) substrate with a 5 nm MgO buffer layer followed by 20 nm of the respective Heusler compound and a 3 nm thick MgO protection layer.

The measurements were carried out at beamline 6.3.1 of the Advanced Light Source of the Lawrence Berkeley Laboratory in Berkeley, California in the USA. The elliptically polarized x-ray beam with a polarization of 66 % hits the sample under a grazing angle of 30 ° while a magnetic field of $\pm$ 1.5 T is applied along the beam direction. From the two obtained spectra I_+ (here the magnetic field and the photon spin are parallel orientated) and I_- (here the magnetic field and the photon spin are anti-parallel aligned) the XAS intensity $(I_+ + I_-)/2$ and the XMCD signal I_+ - I_- can be calculated which give element specific information about the magnetic properties like spin and orbital magnetic moments. In Figure 18 an XAS measurement in total electron yield (TEY) mode is shown. This method measures the sample's photoconductivity as a function of the irradiated photon energy and is surface sensitive thus giving information about the Heusler - MgO interface. The Co_2FeAl sample could also be measured in transmission mode. In this mode the fluorescence spectrum of the pure MgO substrate measured behind the sample is compared to the fluorescence spectrum of the complete sample. In the complete sample the incoming x-ray radiation with certain energies is absorbed resulting in a reduced fluorescence for these energies. The transmission technique is bulk sensitive.

Qualitatively comparing the shape of the absorption curves with the results of Regan et al.[56] one can assume from the marked shoulder on the left side of the Co L_3 maximum for both Heusler samples that a small fraction of Co atoms at the Heusler - MgO interface has absorbed oxygen from the adjacent MgO. Furthermore, a hint of a shoulder can be recognized between the L_3 maxima and the marked features at about 781 eV which fit in their position with parts of the multiplet structure characteristic for CoO. Nevertheless, the multiplet structure is not complete and very unpronounced what indicates an at most weak oxidation of the Co atoms at the interface. The just mentioned shoulder at about 781 eV cannot be assigned to the CoO multiplet structure, but Schmalhorst et al.[57] observe the same feature in their measurements on Co_2MnSi layers with

[56] T. Regan, H Ohldag, *et al.*, *Physical Review B*, vol. 64, p. 214 422, 2001.

[57] J Schmalhorst, S Kämmerer, *et al.*, *Physical Review B*, vol. 70, p. 024 426, 2004.

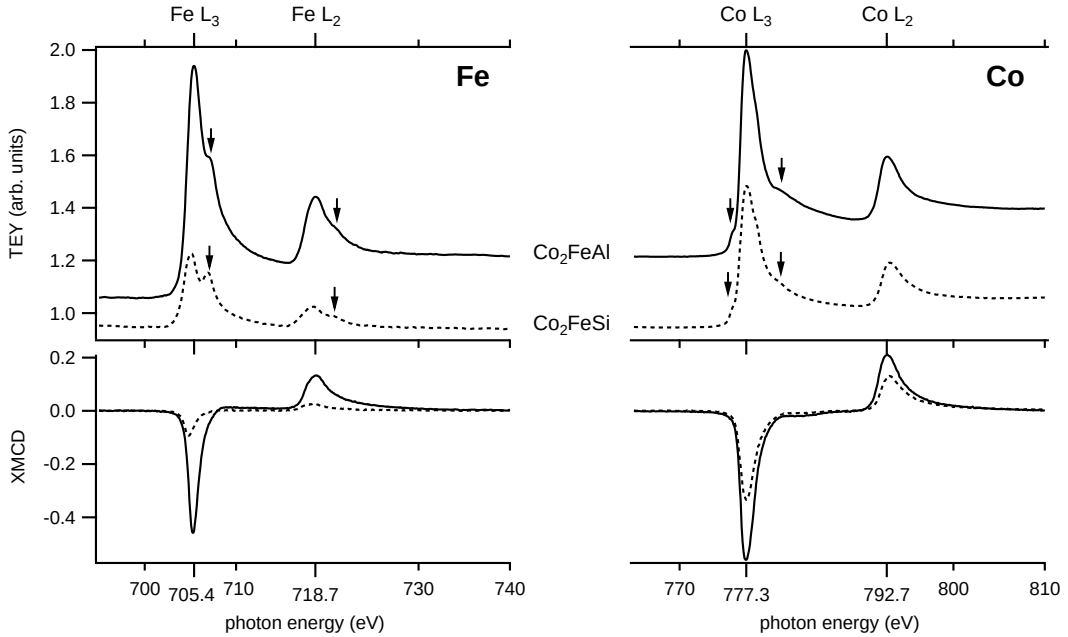

Figure 18: XAS and XMCD spectra of Co_2FeSi (dashed lines) and Co_2FeAl samples (solid line) measured in TEY mode. L_3 and L_2 absorption edges of Fe (left) and Co (right). The marked features in the Fe absorption edges and the left in the Co absorption edges are signs of Fe oxides and Co oxides respectively at the interface while the marked shoulder ~4eV above the Co L_3 absorption maximum originates from a certain atomic and magnetic ordering.

a natively oxidized Al capping layer. They attribute it to a particular atomic as well as magnetic ordering of the Co atoms in their Heusler compound layer. Hence, this observed feature can be interpreted as an indicator for B2 type Heusler ordering which superpositioned with the signal from the partly oxidized Co near the interface results in the observed shape of the XAS spectrum.

Looking at the XAS spectrum in transmission mode (see Figure 19) the same feature as in TEY mode can be observed for Co_2FeAl about 4 eV above the L_3 absorption edge of Co. Compared to the TEY curve (see Figure 18) it is clearer and can also be identified as a shoulder in the L_2 absorption edge, whereas it is at best vaguely perceptible in the TEY case. As the transmission mode is sensitive to absorptions in the whole film our findings imply a long range B2 type ordering of our Co_2FeAl layers. Kallmayer et al.[58] explain the emergence of the feature by a binding of Co d-states to the main group element's sp-states.

However, it has to mentioned that the shape of the feature at

[58] M Kallmayer, H Schneider, *et al.*, *Journal of Physics D: Applied Physics*, vol. 40, pp. 1552–1557, 2007.

781.4 eV is unusual. The steep drop at its right side is commonly not observed and its origin unknown.

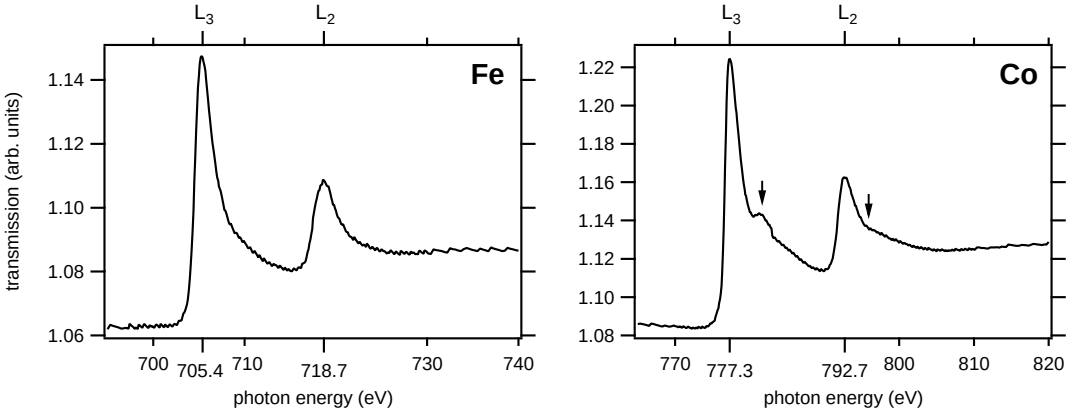

Figure 19: XAS spectra of a Co_2FeAl sample measured in transmission mode. L_3 and L_2 absorption edges of Fe (left) and Co (right).

Considering the Fe L_3 and L_2 absorption edges in TEY mode (see left side of Figure 18) for both Heusler samples the multiplet structure can clearly be identified, particularly in the case of Co_2FeSi. The distance between the double peaks agree quite well with those obtained for different Fe oxides by Regan et al., however the ratios of the double peak intensities are reversed as they find the peak at the lower energy of the L_2 and L_3 absorption edge respectively to be the one with the lower intensity. This leads to the conclusion that our XAS spectra are a superposition of the structureless shape of the $L_{2,3}$ absorption edge typical for metallic Fe and the multiplet structure of Fe oxides. Hence, the Fe atoms at the Heusler - MgO interface are oxidized to some extent. In case of Co_2FeSi the oxidization should be stronger as the double peak shape of the $L_{2,3}$ absorption edge is more pronounced and the ratio of the two neighboring peaks are closer to those of the Fe oxides.[59] This discovery is not really surprising, because the Co_2FeSi sample was not covered with MgO till the in-situ annealing at 935 °C for one hour had been completed, while the Co_2FeAl sample was capped directly after the deposition of the Co_2FeAl layer.

[59] T. Regan, H Ohldag, *et al.*, *Physical Review B*, vol. 64, p. 214422, 2001.

For the bulk sensitive transmission measurement of the Co_2FeAl sample (see left side of Figure 19) the situation is different. Here the Fe $L_{2,3}$ edges do not show any structure as would be expected from metallic Fe. This means the Fe oxidization is limited to the interface region.

From the XAS and XMCD spectra the element specific mag-

Table 1: Magnetic moments of Fe and Co obtained from XAS and XMCD measurements and the theoretically predicted values. The theoretical total magnetic moments deviate slightly from the values one would obtain from $m_{tot} = m_{Fe} + 2m_{Co}$ as they also include small contributions from Al, Si and other corrections.

	Co_2FeAl			Co_2FeSi		
	m_{Fe} (μ_B)	m_{Co} (μ_B)	m_{tot} (μ_B)	m_{Fe} (μ_B)	m_{Co} (μ_B)	m_{tot}
TEY	3.07 ± 0.14	1.78 ± 0.10	6.63 ± 0.24	1.93 ± 0.25	1.81 ± 0.06	5.55 ± 0.41
transmiss.	3.82 ± 0.26	0.91 ± 0.05	5.64 ± 0.29	–	–	–
predicted	2.81^a	1.14^a	5.00^a	3.30^b	1.54^b	6.00^b

[a]: adopted from Galanakis[Galo5], [b]: adopted from Wurmehl et al.[WF+o5]

netic moments can be deduced by applying the sum rules.[60] Table 1 summarizes the obtained magnetic moments of Fe (m_{Fe}), Co (m_{Co}) and the total magnetic moment of a formula unit ($m_{tot} = m_{Fe} + 2m_{Co}$).

The interfacial moments extracted from the TEY data strongly deviate from the theoretically predicted values. In the case of Co_2FeAl the magnetic moment of Fe with $(3.07 \pm 0.14)\,\mu_B$ is only slightly elevated compared to the predicted value of $2.81\,\mu_B$ while the Co magnetic moment of $(1.78 \pm 0.10)\,\mu_B$ is clearly above the theoretical magnitude of $1.14\,\mu_B$. For the bulk moments deduced from the transmission data the situation is inverted. Here the Co moment of $(0.91 \pm 0.05)\,\mu_B$ is quite near the prediction whereas m_{Fe} is elevated with $(3.82 \pm 0.26)\,\mu_B$. Even though the obtained m_{Fe} do not match the predictions, there is a tendency of a reduced surface magnetic moment compared to the bulk value which can be attributed to Fe oxides at the interface. The overestimated total magnetic moment of $6.63\,\mu_B$ and $5.64\,\mu_B$ compared to the predicted $5\,\mu_B$ for the interface and bulk case respectively is reproduced by a value of $5.25\,\mu_B$ obtained from AGM measurements (see Figure 20) and by trend consistent with findings of D. Ebke.[61]

For Co_2FeSi the opposite tendency can be observed considering the magnetic moments at the interface. The Co magnetic moment ($m_{Co} = (1.81 \pm 0.06)\,\mu_B$) is rather near the predicted $1.54\,\mu_B$ and m_{Fe} is explicitly underestimated with only $(1.93 \pm 0.25)\,\mu_B$ compared to the predicted $3.30\,\mu_B$. But this discrepancy can again be explained by the increased content of Fe oxides at the interface just as the high error margin of m_{Fe}.

The overestimation of some magnetic moments is probably due to minor stoichiometric deviations (maybe caused by the

[60] C. Chen, Y. Idzerda, *et al.*, *Physical Review Letters*, vol. 75, no. 1, pp. 152–155, 1995.

[61] D. Ebke, "Cobalt based Heusler compounds in magnetic tunnel junctions", PhD thesis, Bielefeld University, 2010.

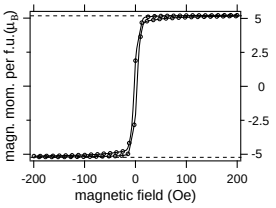

Figure 20: Magnetization curve of a 20 nm thick Co_2FeAl sample obtained from AGM measurements at RT and converted into magnetic moment per formula unit. The coercive field amounts ~ 3 Oe. The dashed lines mark the maximum/minimum total magnetic moment per f.u. of $\pm 5.25\,\mu_B$.

heat treatment) from perfect Co_2FeSi and Co_2FeAl respectively, which in turn affects the number of 3d holes n_d. n_d is an important factor in the calculations and directly alters the obtained moments, so that an oversized n_d results in moments which are systematically too large.

In summary, the structure analysis of the deposited Co_2FeSi (CFS-co and CFS-MLM) thin films by XRD have shown a high B2 type crystal ordering (84 % and 95 % respectively) which, in the case of CFS-MLM, is backed up by a characteristic feature in the XAS spectrum ~ 4 eV above the Co L_3 absorption edge. The multiplet splitting in the XAS spectrum also showed the presence of oxides, particularly of Fe oxides at the interface which are responsible for a clearly reduced surface magnetic moment of the Fe atoms. From AGM measurements a reduced magnetic moment of up to $3.64\,\mu_B$ and $4.94\,\mu_B$ per formula unit compared to a theoretically predicted value of $6\,\mu_B$ could be deduced for CFS-co and CFS-MLM respectively. The also observed increase of the coercive field for elevated annealing temperatures was attributed to a growth of the crystallite size within the film for both fabrication techniques. As AFM studies revealed a higher surface roughness of the CFS-co samples the MBE multilayer method will be employed for further studies to produce Heusler based MTJs.

As second Heusler compound sputtered Co_2FeAl will be employed as lower magnetic electrode, which has been studied extensively within our workgroup and has yielded TMR amplitudes of up to 147 % at RT.[62] In the XAS spectra (surface sensitive TEY and bulk sensitive transmission) the same ordering feature as with Co_2FeSi could be observed for Co and a comparison of the TEY and transmission mode spectra indicate that the slight oxidation of Fe atoms is limited to the upper surface of the layer. The element specific magnetic moment extracted from the XAS and XMCD measurements show at least that these Fe oxides significantly reduce the Fe magnetic moments at the surface compared to the bulk, even though they are still overestimated.

[62] D. Ebke, P. Thomas, *et al.*, *Journal of Magnetism and Magnetic Materials*, vol. 322, no. 8, pp. 996 –998, 2010.

Barium Oxide

This chapter will introduce BaO and present its properties concerning its use in MTJs as a tunneling barrier. Besides the crystallographic and chemical characteristics the electronic properties will be considered. Afterwards, the experimental realization of the first BaO layers will be covered and the obtained results including XRD analysis and AFM surface roughness measurements presented. In doing so the difficulties concerning the practical handling of BaO will be pointed out.

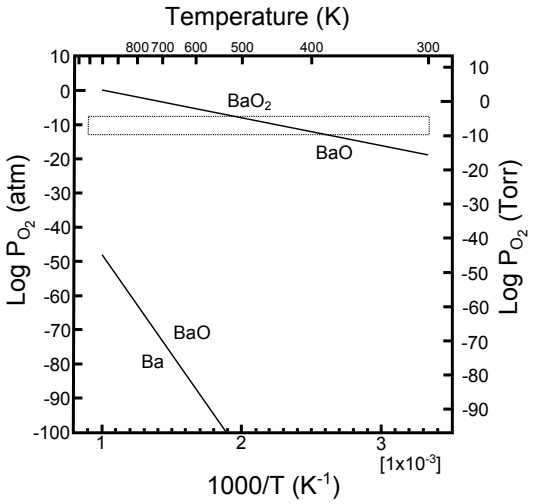

Figure 21: Stability diagram of the Ba - BaO - BaO_2 system. Depicted from [OY+97].

Barium is an alkaline earth metal with *Ba* as chemical symbol and atomic number 56. Ba can not be found elemental in nature due to its high reactivity. Also BaO is unstable. On the one hand at atmospheric pressure BaO_2 is the stable oxide phase (see Figure 21) and on the other hand BaO is very hygroscopic, so that the moisture in the air is rapidly absorbed and barium

hydroxide is formed.

$$BaO + H_2O \longrightarrow Ba(OH)_2$$

BaO has an fcc crystal structure with a experimental lattice constant of $a = 5.53\,\text{Å}$ and an experimentally obtained lattice energy between 730.9 kcal/mol (31.69 eV) and 749.2 kcal/mol (32.49 eV).[63] Calculations by Lv et al.[64] suggest BaO to show a bandgap of $E_G = 2.056\,\text{eV}$ when using *local density approximation (LDA)* while the *GW approximation (GWA)*[65] gives $E_G = 3.907\,\text{eV}$. The latter value is in good agreement with results from optical absorption spectra of polycrystalline BaO films at $T = -160\,^\circ\text{C}$ of $E_G = 3.88\,\text{eV}$[66] and at RT of $E_G = 4.10\,\text{eV}$.[67] Thus BaO lies right on the borderline between semiconductor and insulator and meets the requirements for being utilized as a tunneling barrier.

[63] R. Meyer and E. Pietsch, *Gmelins Handbuch der anorganischen Chemie: Barium Ergänzungsband*, 30. Verlag Chemie, 1960.

[64] T. Lv, D. Chen, *et al.*, *Journal of Applied Physics*, vol. 100, p. 086 103, 2006.

[65] G: Green's function W: screened Coulomb interaction

[66] R. Zollweg, *Physical Review*, vol. 111, no. 1, pp. 113–119, 1958.

[67] G. Saum and E. Hensley, *Physical Review*, vol. 113, no. 4, pp. 1019–1022, 1959.

[68] T. Ohnishi, M. Yoshimoto, *et al.*, *Journal of Vacuum Science & Technology A: Vacuum, Surfaces, and Films*, vol. 15, no. 5, pp. 2469–2472, 1997.

First BaO layers

We decided to fabricate our BaO layers by evaporating pure Ba metal in a low O_2 atmosphere as Ohnishi et al. have demonstrated.[68] The 99.9 % pure Ba metall pieces, which had been delivered in mineral oil for protection, were cleaned with Hexane in a glovebox under inert gas following a strict cleaning protocol. After the six cleaning cycles the Ba pieces were transferred into a Molybdenum crucible still within the glovebox and afterwards packed air tight.

The crucible was installed into the custom made Knudsen cell (see Appendix for construction details) and the MBE chamber while the MBE chamber was under excess pressure of Ar to minimize the exposure of the Ba with O_2 or H_2O from the atmosphere.

The first step was to find the correct growth parameters[69] to actually get BaO and not BaO_2, cubic or hexagonal Ba. Therefore the influence of T_{sub} and p_{O_2} on the resulting BaO_x layers has been systematically investigated for a fixed evaporation rate and layer thickness. Based on the phase diagram of the Ba - BaO - BaO_2 system (see Figure 21) T_{sub} was chosen to be varied between 250 °C and 400 °C and p_{O_2} between 5×10^{-7} mbar and 5×10^{-6} mbar.

[69] The crucial growth parameters are the substrate temperature T_{sub} and the O_2 pressure p_{O_2}.

For all samples of this series Si substrates with a 50 nm native oxide layer are used which are first deposited with a 5 nm MgO buffer layer by RF magnetron sputtering. Afterwards the samples are transferred into the MBE chamber and in-situ annealed

at 500 °C for 10 minutes. Afterwards they are cooled down to the respective T_{sub}. As the annealing temperature is above the highest investigated T_{sub} it is ensured that the texture of the MgO buffer layer is approximately the same for all samples and that the obtained BaO results are not influenced by differing degrees of MgO crystallinity induced by T_{sub} itself. When the desired substrate temperature is reached p_{O_2} is adjusted using a high precision needle valve and the deposition process is started. As soon as the Ba shutter is opened the Ba binds to the O_2 and the pressure decreases rapidly which has to be compensated by increasing the O_2 flux until p_{O_2} is adjusted again. When the deposition process is finished the O_2 flow is stopped, the substrate cooled down and the samples transferred into the sputtering system again to be finished by a 10 nm MgO protection layer. Directly after the removal of the samples from the load lock the edge, where the substrate has been clamped to the substrate holder, is sealed with conducting silver in order to prevent moisture from soaking into the BaO layer. In addition a reference sample without a BaO layer was deposited with the same MgO layers, heat treatment, and conducting silver. The XRD reflections measured on this reference sample can then be excluded from the evaluation of the samples containing BaO.

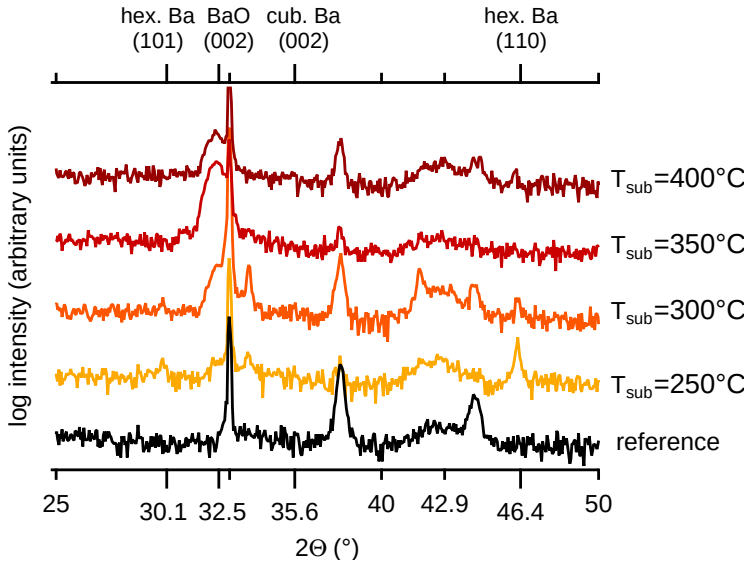

Figure 22: XRD spectra of MgO(5 nm)/BaO/MgO(10 nm) samples deposited on SiO_x substrates at different T_{sub} during BaO growth and a reference sample without BaO layer. The O_2 pressure during the BaO growth was 5×10^{-7} mbar.

Figure 22 shows the XRD spectra of BaO samples grown at $p_{O_2} = 5 \times 10^{-7}$ mbar and different T_{sub}. Furthermore, the spectrum of the reference sample is shown. The sharp Si(002) peak at 33 ° can be attributed to the doping of the Si substrate which causes the – in case of undoped Si forbidden – (002) reflection to appear. The peak at 42.9 ° is the MgO(002) reflection while the peaks at 38.1 ° and 44.3 ° are caused by the conducting silver.[70] The important and designated reflection is the BaO(002) peak at 32.5 ° for cubic BaO which shows the highest intensity at $T_{sub} = 350\,°C$. At the same time there are no further peaks visible that could be attributed to other Ba or BaO_x phases like Ba(101) at 30.1 ° ($T_{sub} = 250\,°C$ and $T_{sub} = 300\,°C$) and Ba(110) at 46.4 ° ($T_{sub} = 250\,°C$, $T_{sub} = 300\,°C$, and $T_{sub} = 400\,°C$) for hexagonal Ba or Ba(002) at 35.6 ° for cubic Ba. The reflection at $\sim 30.9\,°$ cannot definitely be identified, but could be caused by a small amount of $BaO_{1.3}$.[71] The peaks at $2\theta = 33.8\,°$ and $2\theta = 41.7\,°$ most prominent in the $T_{sub} = 300\,°C$ curve cannot be attributed to any Ba, BaO or BaO_2 peak and is likely caused by an unknown oxidation state of BaO_x. The differences in the peak intensities caused by the conducting silver is purely due the position of the area covered with conducting silver in the x-ray beam.

[70] The conducting silver as origin of the mentioned reflections could be identified by measuring the reference sample before and after applying the conducting silver and comparing the spectra.

[71] T. Jondo, R. Abraham, *et al.*, *Journal of alloys and compounds*, vol. 186, no. 2, pp. 347–359, 1992.

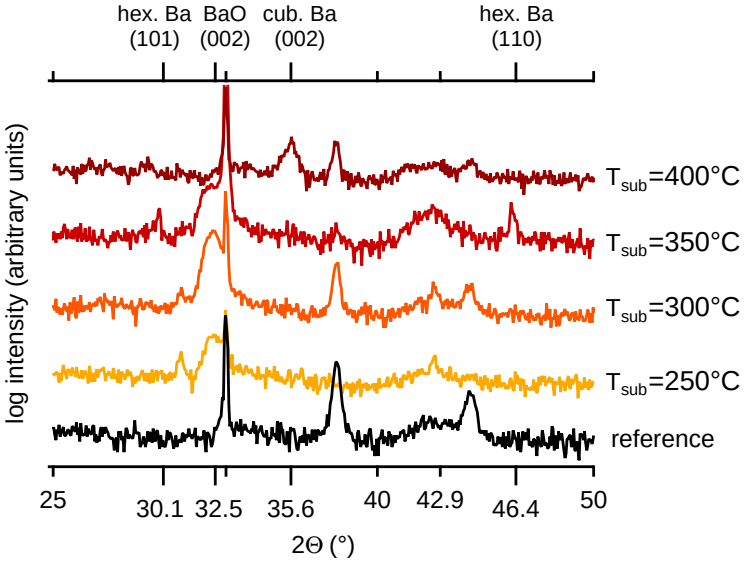

Figure 23: XRD spectra of MgO(5 nm)/BaO/MgO(10 nm) samples deposited on SiO_x substrates at different T_{sub} during BaO growth and a reference sample without BaO layer. The O_2 pressure during the BaO growth was 1×10^{-6} mbar.

For $p_{O_2} = 1 \times 10^{-6}$ mbar (see Figure 23) a substrate temperature of 300 °C delivers the BaO layers with the strongest BaO(002) while reflections of cubic or hexagonal Ba are absent. The curve is very similar to the spectrum of the sample grown at $p_{O_2} = 5 \times 10^{-7}$ mbar and $T_{sub} = 350$ °C, even the small reflection at $2\theta = 30.9°$ is comparable in area and height. The net areas of the BaO(002) peak are virtually identical for both curves with 226 and 230 counts per second (cps), particularly if considering the overlying Si(002) reflection.
Other substrate temperatures result in a reduced BaO(002) intensity ($T_{sub} = 250$ °C), a mixed phase of BaO and hexagonal Ba ($T_{sub} = 350$ °C) or only cubic Ba ($T_{sub} = 400$ °C).

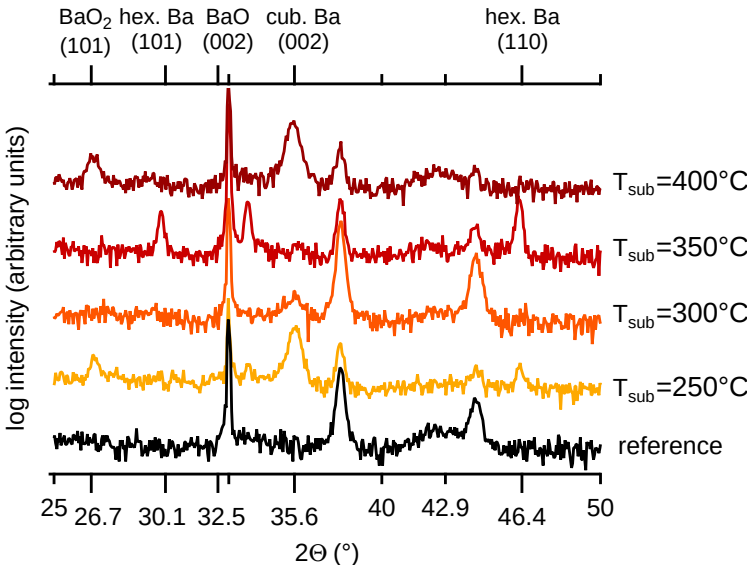

Figure 24: XRD spectra of MgO(5 nm)/BaO/MgO(10 nm) samples deposited on SiO_x substrates at different T_{sub} during BaO growth and a reference sample without BaO layer. The O_2 pressure during the BaO growth was 5×10^{-6} mbar.

For $p_{O_2} = 5 \times 10^{-6}$ mbar (see Figure 24) there is no BaO(002) reflection in the whole investigated temperature range. For $T_{sub} = 250$ °C and $T_{sub} = 400$ °C the BaO_2(101) peak arises which is by tendency in agreement with the pressure dependence of the Ba - BaO - BaO_2 system shown in Figure 21. The reflection of unknown origin can again be observed at $2\theta = 33.8°$ for $T_{sub} = 350$ °C.

The BaO(002) peak is generally found at slightly smaller diffraction angles compared to the literature which means a small increase of the out-of-plane lattice constant. Furthermore,

the absent of the BaO(111) peak at 27.9 °, which is the dominant reflection in polycrystalline BaO samples, implies the existence of the favored (001) texture.

The thickness measurement turned out to be very demanding. To be able to obtain the thickness by *x-ray reflection (XRR)* measurement the film should be at least 10 nm thick and BaO layers tend to be quite rough, so that even with a protection layer there are spots where the BaO lies free. Due to the high reactivity of BaO these areas are sufficient to allow the whole BaO layer to form barium hydroxide within minutes. Hence the resulting XRR measurements were very difficult to evaluate and the thickness could only be determined with a high error margin. Alternatively the layer thickness could be measured by *atomic force microscopy (AFM)*, but this would require a clean edge at which the layer thickness could be measured by determining the difference in the levels before and behind the edge. However, this edge is realized as a result the BaO would always be exposed to the atmosphere and influence the obtained thickness. After weighing up the errors of both techniques the XRR measurement was chosen to determine the BaO layer thickness.

A quartz crystal thickness monitor which was used while the calibration samples were deposited was then adjusted considering the obtained values from the XRR measurement. Thereby it was not necessary to repeat the thickness measurement by means of XRR for every evaporation temperature and hence deposition rate as the thickness monitor was employed to determine the particular BaO barrier thickness of the fabricated TMR layer stack. Nevertheless, the specified BaO layer thicknesses should be regarded with caution in the following. That is also the reason why it was not meaningful to systematically investigate the BaO layer thickness dependence on the MTJ's properties.

Due to the high roughness of the thicker BaO films investigated for the thickness calibration AFM measurements on a thin BaO film of 3 nm deposited on SiO_x substrate and covered by a 5 nm MgO layer was carried out (see Figure 25 a) to be sure that it could be employed as a tunneling barrier. Completingly, the roughness of the MgO protection layer alone was determined (see Figure 25 b). With $R_{\mathrm{RMS,BaO}} = 0.24\,\mathrm{nm}$ for the BaO layer with MgO capping the thin BaO layer is smooth enough to be used as a barrier layer particularly when considering $R_{\mathrm{RMS,MgO}} = 0.12\,\mathrm{nm}$ for the MgO capping layer alone.

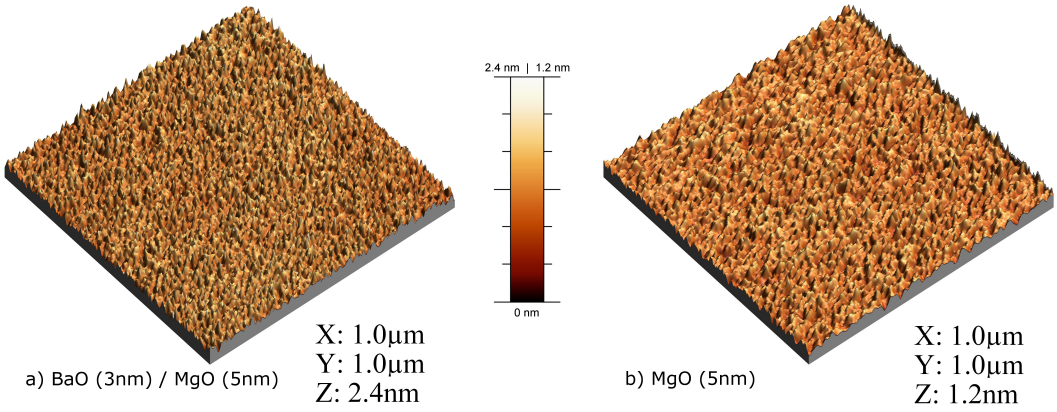

Figure 25: 3D illustration of AFM measurements on: a) BaO (3 nm) / MgO (5 nm) and b) MgO (5 nm). Both samples were deposited on SiO_x substrate.

In summary, the crucial properties regarding the applicability of BaO as a tunneling barrier in Heusler based MTJs like lattice structure, lattice parameter and conductivity make BaO an ideal candidate for a novel barrier material. From XRD studies a narrow temperature and pressure window could be determined for which crystalline BaO is formed. The findings are summarized in Figure 26. Although XRR measurements on thicker BaO layers (> 10 nm) have shown a high surface roughness, AFM measurements on thin layers applicable for tunneling barriers have revealed a sufficient surface smoothness. Nevertheless, the high reactivity of BaO complicates the practical use of it and means a challenging task.

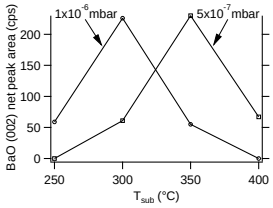

Figure 26: Net peak areas of the Ba(002) XRD reflections as a function of T_{sub} for $p_{O_2} = 5 \times 10^{-7}$ mbar and $p_{O_2} = 1 \times 10^{-6}$ mbar.

Co_2FeSi based MTJs

This chapter will address Co_2FeSi based MTJs with a BaO tunneling barrier. It will start with the preparation of the TMR layer stack and will further cover experimental results from transport measurements. In particular the bias and temperature dependence of the TMR ratio will be discussed and comparisons to MgO based MTJs will be drawn. In addition, the findings will be supported by noise measurements to look into the origin of the observations.

Even though the lattice mismatch of Co_2FeSi with respect to MgO is only about 5 %, Heusler based MTJs have not yet exceeded CoFeB based MTJs with regard to their TMR amplitude. As the Heusler compounds' spin polarization is very sensitive to crystal defects, this small mismatch could be responsible for the reduced TMR effect.

From self-consistent first principle calculations Block et al.[72] find for the Co based Heusler compound Co_2CrAl that uniform strain beyond $-1\,\%$ and $+3\,\%$ destroys the half metallic properties mainly due to a shift of E_F away from the gap. Also tetragonal distortion exceeding $\pm 2\,\%$ lowers the spin polarization primarily by closing E_{gap}. The same group draws similar conclusions for Co_2MnGe which sustains its half metallicity for tetragonal distortions within $0\,\%$ and $+4\,\%$ and uniform strain in the range of $-2\,\%$ and $0\,\%$.[73] If these results are transferable to other (Co based) Heusler compounds, finding a lattice matched barrier material for MTJs with a Heusler electrode will potentially yield higher spin polarizations and consequently higher TMR ratios as well.

Hence, we have introduced BaO as a new barrier material for Heusler based MTJs. The lattice mismatch of BaO ($a = 5.53\,\text{Å}$) with respect to Co_2FeSi ($a = 5.66\,\text{Å}$) is less than 3 %, hence offering better conditions for defect free crystal growth at the Co_2FeSi/BaO interface. Therefore, one goal in this work has been to fabricate MTJs with a Co_2FeSi lower electrode and a BaO

[72] T. Block, M. Carey, *et al.*, *Physical Review B*, vol. 70, no. 20, pp. 1–5, 2004.

[73] M. J. Carey, T. Block, *et al.*, *Applied Physics Letters*, vol. 85, no. 19, pp. 4442–4444, 2004.

tunneling barrier to prove that BaO can be grown epitaxially on Co_2FeSi (001) and that a BaO based MTJ shows a TMR effect at all.

Sample Preparation

For all samples MgO(001) substrates are used which are coated with a 5 nm thick MgO buffer layer by RF magnetron sputtering. The 15 nm thick Co_2FeSi electrodes have been fabricated employing the multilayer MBE method which has been introduced in section Heusler sample preparation on page 21. In contrast to the CFS-MLM samples the number of iterations is reduced to 25 and the annealing temperature is set to 935 °C even though the best results were obtained with $T_a = 950\,°C$. The temperature has been reduced because the slightly lower annealing temperature does not alter the crystal structure and as 950 °C is near the maximum temperature the substrate holder heater can achieve, the last 15 K take a much longer time to be overcome. Before the barrier growth is started a very thin (~ 0.1 nm) Ba layer is deposited to avoid the formation of FeO on the Heusler surface due to the oxygen atmosphere required for the BaO growth. The BaO barrier layer is then deposited by evaporating barium metal under low oxygen pressures of 1×10^{-6} mbar at substrate temperatures of 300 °C according to the results presented in chapter Barium Oxide. The aimed barrier thickness is between 2.9 nm and 3.1 nm. Finally the 20 nm thick Fe top electrode is deposited by MBE, followed by a Ta(5 nm) / Au(50 nm) capping, which is sputtered ex-situ. Figure 27 shows the layer system schematically.

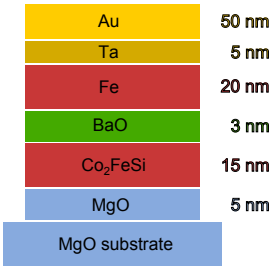

Figure 27: Schematic drawing of the fabricated TMR layer stack.

Afterwards electron beam lithography techniques and Ar ion beam etching are employed to structure elliptical shaped MTJs. The ellipses are produced with four different dimensions: $(6 \times 2)\,\mu m^2$, $(3 \times 1)\,\mu m^2$, $(1 \times 0.3)\,\mu m^2$ and $(0.6 \times 0.2)\,\mu m^2$. With this design of the MTJs a partly antiparallel alignment of the electrodes' magnetizations is favored without an outer magnetic field due to dipole coupling. This pinning is not as strong and stable as exchange biased layers involving antiferromagnets[74] and does not shift the hysteresis loop. Furthermore the MTJs' magnetic easy axes are parallel to the ellipses' major axes because of shape anisotropy. The structured samples have to be sealed directly after the etching process by filling up the empty space with TaO_x in order to protect the sensitive BaO barrier from atmospheric moisture.

[74] J. Nogués and I. K. Schuller, *Journal of Magnetism and Magnetic Materials*, vol. 192, pp. 203–232, 1999.

In section "Results" on page 24 it has been shown that B2 ordered Co_2FeSi layers could be produced and it can furthermore be assumed from the previously presented findings on BaO layers on MgO(001) that BaO layers with (001) texture are also grown if deposited on the Co_2FeSi (001) surface. Particularly considering the much better lattice matching the Co_2FeSi offers ideal growth conditions for (001) texture of the BaO layer. XRD measurements on a complete Co_2FeSi/BaO/Fe TMR stack would not show the BaO (002) peak, because the intensity would be very low due to the reduced layer thickness of $\sim 3\,\mathrm{nm}$. In addition the lattice parameters of BaO and Co_2FeSi are so close that their respective (002) reflections could not be distinguished from each other. This effect is further supported by a slight stretching of the BaO lattice to fit the one of Co_2FeSi.

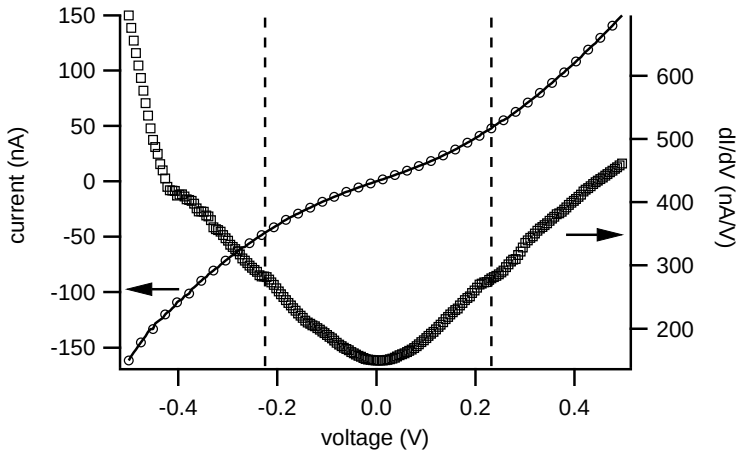

Figure 28: *I-V* measurement (left axis, circles) on a $(3 \times 1)\,\mu m^2$ Co_2FeSi/BaO/Fe MTJ and the numerically deduced dI/dV curve (right axis, squares).

The transport measurements have been done in conventional two-point geometry and the magnetic field is applied along the MTJs' easy axes. During these measurements the BaO based MTJs turned out to be very unstable. That means they regularly broke down after the first measurement which seriously complicated a systematic characterization.

Figure 28 shows the *I-V* curve measured without an applied magnetic field on a $(3 \times 1)\,\mu m^2$ MTJ (area resistance product $RA \approx 300\,k\Omega\mu m^2$) with the characteristic shape for an involved tunneling process. The same figure also includes the dI/dV

curve, which has been numerically deduced from the *I-V* measurement and also possesses the expected form except for the conductance reduction at ±230 mV (marked with dashed vertical lines) and −400 mV. Miao et al.[75] as well as Matsumoto et al.[76] observe a similar symmetric dip structure at ±300 mV on their CoFeB/MgO(001)/CoFeB MTJs. They only observe these characteristics for (001) textured crystalline electrodes and MgO barrier and attribute them to coherent tunneling. Also MTJs containing the Heusler compound Co_2MnSi have shown such a feature at ±400 mV,[77] so that we can assume the found dI/dV curve shape to evidence crystalline electrodes as well as BaO barrier and hence coherent tunneling.

[75] G.-X. Miao, K. B. Chetry, *et al.*, *Journal of Applied Physics*, vol. 99, no. 8, 08T305, 2006.

[76] R. Matsumoto, S. Nishioka, *et al.*, *Solid State Communications*, vol. 143, pp. 574 –578, 2007.

[77] S. Tsunegi, Y. Sakuraba, *et al.*, *Applied Physics Letters*, vol. 93, no. 11, p. 112 506, 2008.

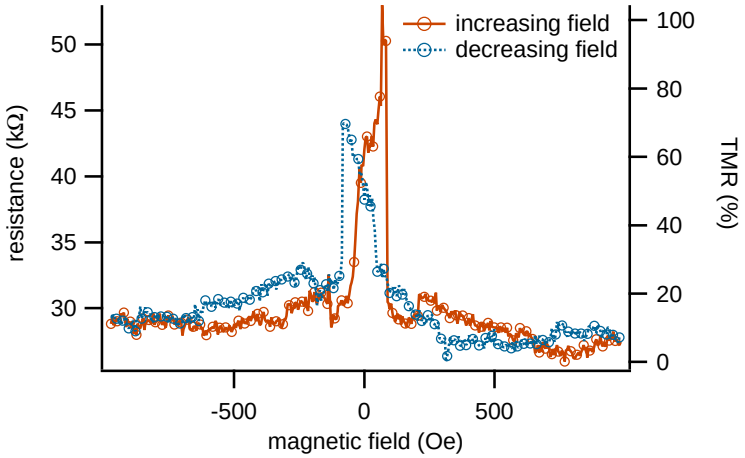

Figure 29: TMR measurement on a Co_2FeSi/BaO/Fe MTJ with $V_{Bias} = 0.1$ mV at RT. The left axis shows the absolute resistance, while the right axis displays the equivalent TMR amplitude.

The TMR amplitude is strongly V_{Bias} dependent and increases with decreasing V_{Bias}. Figure 29 shows the TMR measurement of a $(3 \times 1)\,\mu m^2$ MTJ with an applied V_{Bias} of 0.1 mV and a TMR ratio of about 100 %. The same MTJ exhibits 60 % with $V_{Bias} = 0.2$ mV (see Figure 30) and only 14 % with $V_{Bias} = 10$ mV (see Figure 31). From the TMR loop in Figure 30 one electrode seems to be exchange biased, but this is an effect of low magnetic stability. The magnetically harder Fe layer does not switch its magnetization in the exact same way each time the magnetic field crosses zero field. In Figure 29 for both increasing and decreasing magnetic field the Fe layer's magnetization switches instantly resulting in a narrow TMR loop. In contrast to this, in Figure 30 for the decreasing field the Fe layer's magne-

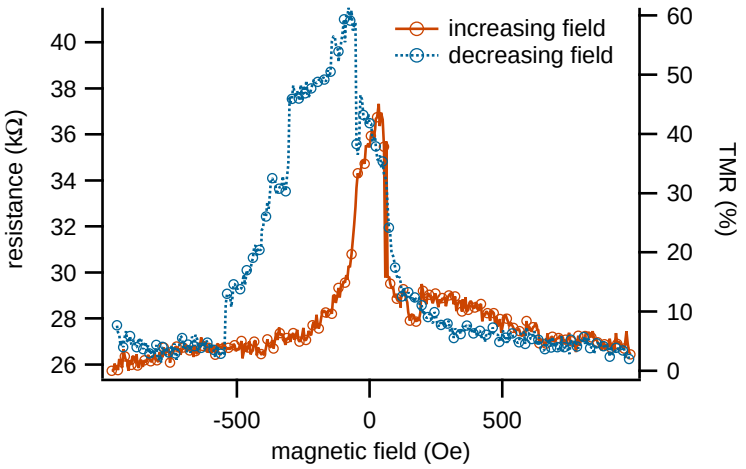

Figure 30: TMR measurement on a $Co_2FeSi/BaO/Fe$ MTJ with $V_{Bias} = 0.2\,mV$ at RT. The left axis shows the absolute resistance, while the right axis displays the equivalent TMR amplitude.

tization switches over a broader field range. There are magnetic domains within the Fe layer turning one by one and yielding the exchange biased like shape of the TMR loop. Neither is the switching behavior bias dependent as could be assumed from the TMR loops.

The normalized TMR (TMR/TMR_{max}) vs. V_{Bias} dependence is displayed by the red, solid line in Figure 32. As can be seen from the error bars, the uncertainty in the measurement also grows with dropping V_{Bias}. This is mainly due to the voltage variations the power supply unit delivers, which become more dominant for very small bias voltages. To exclude that any malfunction of the used measurement setup causes the seeming high TMR ratios at low V_{Bias} we have also measured a $Co_2FeSi/MgO/CoFe$ MTJ with comparable resistance, TMR ratio ($TMR_{max} = 110\,\%$) and identical adjustments of the measurement setup (see the black, dashed line in Figure 32). The $Co_2FeSi/MgO/CoFe$ MTJ merely shows the usual slight increase of TMR ratio with decreasing V_{Bias}.

Figure 33 illustrates this rise in TMR with decreasing V_{Bias}. While R_p (blue line) stays more or less constant in the investigated voltage range, R_{ap} (red line) strongly grows with decreasing V_{Bias}.

The extraordinary strong bias voltage dependence compared to MTJs with an MgO barrier cannot be fully explained, but one approach is that defects in the BaO barrier results in two-

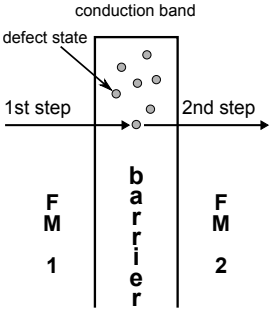

Figure 34: Schematic illustration of the two-step tunneling from ferromagnet 1 (FM 1) via a defect state in the barrier into ferromagnet 2 (FM 2).

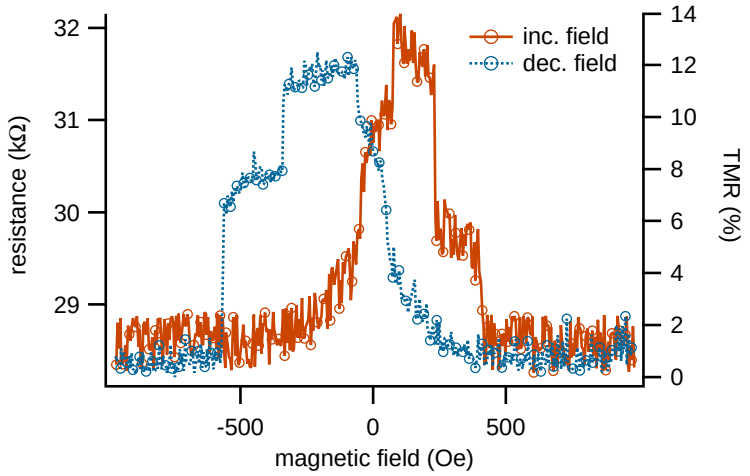

Figure 31: TMR measurement on a $Co_2FeSi/BaO/Fe$ MTJ with $V_{Bias} = 10\,mV$ at RT. The left axis shows the absolute resistance, while the right axis displays the equivalent TMR amplitude.

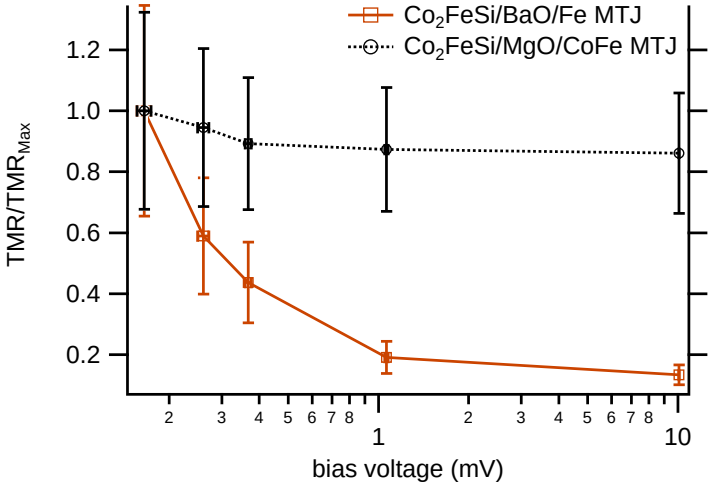

Figure 32: V_{Bias} dependent normalized TMR ratio (TMR/TMR_{max}) of a $Co_2FeSi/BaO/Fe$ MTJ (red, solid line) and a $Co_2FeSi/MgO/CoFe$ MTJ (black, dashed line).

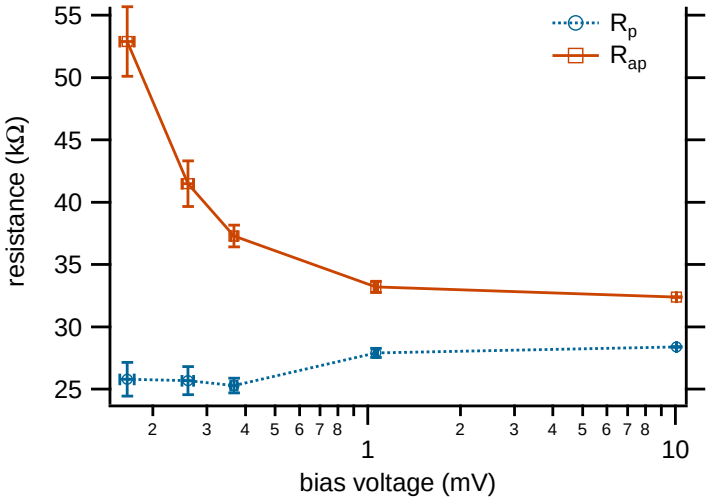

Figure 33: R_p (blue line) and R_{ap} (red line) plotted separately against V_{Bias}.

(or even multiple-) step tunneling and a reduced TMR ratio for increased voltages like Zhang and White have suggested (see schematic in Figure 34).[78] Because the spin independent two-step tunneling current quickly increases with rising voltages, in contrast to the direct tunneling current, it dominates at high voltages reducing the TMR ratio. However, at low voltages the two-step tunneling contribution to the overall current is small yielding the observed high TMR ratio.

We have carried out noise measurements on other samples with BaO barrier support this assumption. For these measurements the current noise was measured directly using a low noise transimpedance amplifier setup. Figure 35 shows the typical slope of pure $1/f$ noise and the transition to thermal noise towards higher frequencies. The $1/f$ noise shows the expected rise with the bias voltage and the derived Hooge parameter has a value of about $4.5 \times 10^{-6}\ \mu m^2$. This value is in the upper range of MTJs with AlO_x barrier and more than three orders of magnitude above the level of low noise MgO based MTJs.[79] Since no field dependence of the noise was observed its origin is purely electronic, indicating a high defect rate either at the interface (most likely in the form of FeO or CoO) or in the barrier itself, e.g. due to oxygen vacancies.

[78] J. Zhang and R. M. White, *Journal of Applied Physics*, vol. 83, no. 11, p. 6512, 1998.

[79] Z. Q. Lei, G. J. Li, *et al.*, *IEEE Transactions on Magnetics*, vol. 47, no. 3, pp. 602–612, 2011.

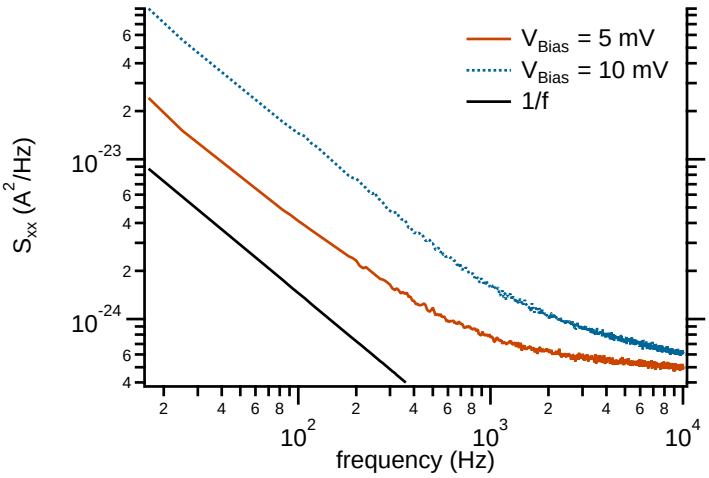

Figure 35: Power spectral density for applied voltages of 5 mV (red, solid line) and 10 mV (blue, dashed line), 50 Hz and harmonics from the mains voltage are cut out.

Low Temperature Measurements

The highest TMR ratio for MTJs with a Heusler electrode of 1995 % has been achieved at 4.2 K with a $Co_2Mn_{1.35}Si_{0.88}/MgO/Co_2Mn_{1.35}Si_{0.88}$ MTJ.[80] This brings up two interesting aspects. The first is that the giant TMR ratio is only measurable at low temperatures and reduces to 330 % at RT. This observation could originate from a reduction of the thermal smearing of k_BT at low temperatures which – particularly if E_F is close to the conduction or valence band – causes a break of the half metallicity at elevated temperatures.[81] But there are also other effects that could contribute and which are still controversially discussed. Shang et al.[82] suggest to complement Jullière's model[83] with a temperature dependent spin polarization due to thermally excited spin waves. The spin polarization has the same temperature dependence as the surface or interface magnetization following *Bloch's law* with a $T^{3/2}$ proportionality. MacDonald at al.[84] demonstrate the relation between the magnetization and spin polarization deducing

$$TMR(T) = TMR(T = 0\,\mathrm{K})(1 - AT^{3/2} + \cdots) \qquad (5)$$

where A denotes the *spin-wave parameter* of the interface. Hagler et al.[85] additionally introduce a spin-independent but temperature dependent conductance channel mostly aroused by hopping conductance through trapped states in the barrier which

[80] H.-X. Liu, Y. Honda, *et al.*, *Applied Physics Letters*, vol. 101, no. 13, p. 132 418, 2012.

[81] J. Akerman, I. Roshchin, *et al.*, *EPL (Europhysics)*, vol. 63, no. 1, pp. 104–110, 2003.

[82] C. Shang, J. Nowak, *et al.*, *Physical Review B*, vol. 58, no. 6, R2917–R2920, 1998.

[83] M. Jullière, *Physics Letters A*, vol. 54, pp. 225–226, 1975.

[84] A. MacDonald, T. Jungwirth, *et al.*, *Physical Review Letters*, vol. 81, no. 3, pp. 705–708, 1998.

[85] T. Hagler, R. Kinder, *et al.*, *Journal of Applied Physics*, vol. 89, no. 11, p. 7570, 2001.

increases the total conductance but reduces the TMR ratio. Another mechanism reducing the TMR ratio for increased temperatures is *spin flip scattering* in the barrier by magnetic impurities. The number of electrons involved in this process grows with rising temperatures[86] which enhances the conductance – particularly for the antiparallel state of the electrodes' magnetizations – and hence reducing the TMR ratio. Other suggestions include hot electrons exciting magnons at the ferromagnet - barrier interface[87] or inelastic scattering, if there are localized states in the barrier.[88] Also the already above given *two-step tunneling*[89] – responsible for a strong bias-dependence of the antiparallel resistance and hence TMR ratio in BaO based MTJs – is temperature dependent and can consequently contribute to the observed effect.

The second interesting aspect is the off-stoichiometry which seems to be crucial for the high TMR ratio as the respective findings of Yamamoto et al. for stoichiometric Co_2MnSi are approximately 875 % at 4.2 K and about 160 % at RT. This substantiates the prospect of tuning also other Heusler (particularly Co_2FeSi) electrode's properties according to one's needs by stoichiometry variations and thus improving the TMR ratio.

Temperature dependent transport measurements have been carried out on $Co_2FeSi/BaO(3.2\,nm)/Fe$ MTJs. In contrast to the MTJs which the measurements presented in the previous section were carried out on, here the MTJs have a quadratic shape (see Figure 36) and the structuring have been done employing optical lithography. After Ar ion beam etching, TaO_x sputtering, and lift-off, the contact pads are written using a second UV-mask (see Figure 37). As this is a lift-off mask, the next step after the development is the sputtering of Ta(5 nm) and Au(50 nm) and eventually the lift-off process reveals the ready-to-measure sample. Figure 38 shows the normalized TMR ratios obtained at low temperatures.

The TMR ratio decreases with increasing temperature as well as the resistance. Looking at the resistances in the parallel (R_p) and antiparallel state (R_{ap}) separately (see Figure 39) it stands out, that R_{ap} has a stronger temperature dependence than R_p which is in agreement with the findings in the literature.

Fitting the raw data from Figure 38 with an equation of the form $A + Bx^C$ according to Equation 5 gives $A = 19.13\,\% \pm 2.98\,\%$, $B = -4.28 \pm 2.17$,[90] and $C = 0.23 \pm 0.06$ or in the nota-

[86] A Vedyayev, D Bagrets, *et al.*, *Physical Review B*, vol. 63, no. 6, p. 064 429, 2001.

[87] S. Zhang, P. Levy, *et al.*, *Physical Review Letters*, vol. 79, no. 19, pp. 3744–3747, 1997.

[88] E. Tsymbal, V. Burlakov, *et al.*, *Physical Review B*, vol. 66, no. 7, pp. 3–6, 2002.

[89] J. Zhang and R. M. White, *Journal of Applied Physics*, vol. 83, no. 11, p. 6512, 1998.

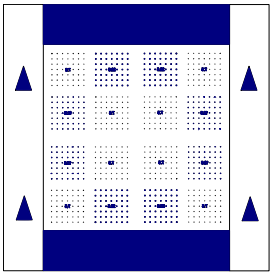

Figure 36: UV lithography mask to structure squarish MTJs with 3 different sizes: $(7.5 \times 7.5)\,\mu m^2$, $(12.5 \times 12.5)\,\mu m^2$, and $(22.5 \times 22.5)\,\mu m^2$.

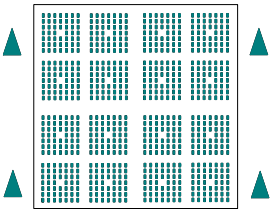

Figure 37: UV lithography mask to structure the contact pads. The triangles on the sides are aligned with those on the sample to correctly position the contact pads on the MTJs.

[90] The units of B are omitted for clarity reasons. Assuming a $T^{3/2}$ dependence the dimension of B would be $1\,\%K^{3/2}$.

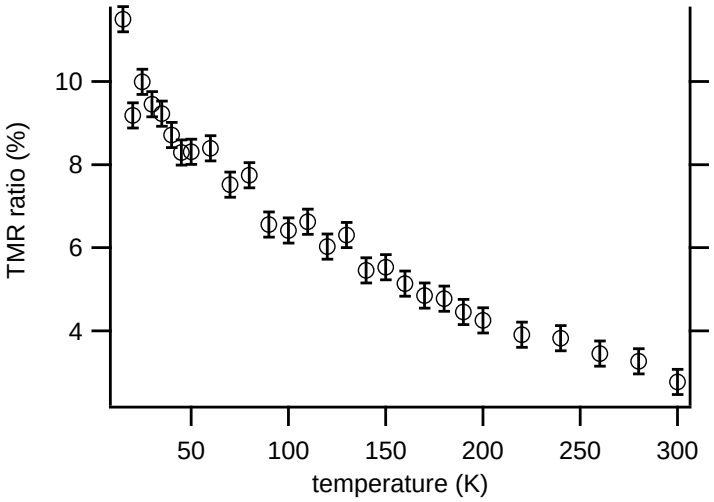

Figure 38: Temperature dependence of the normalized TMR ratios for $Co_2FeSi/BaO(3.2\,nm)/Fe$ MTJs at $V_{Bias} = 10\,mV$.

tion of Equation 5

$$TMR(T) = (19.13 \pm 2.98)\,\% \cdot (1 - (0.22 \pm 0.12)\mathrm{K}^{-3/2} \cdot T^{0.23\pm0.06}).$$

Hence, spin wave excitation does not govern the observed temperature dependence of the TMR ratio as the exponent from the fit does not match the predicted $T^{3/2}$ proportionality at all.

To have a closer look at the temperature dependence of the TMR ratio the conductance will be focused. Shang et al.[91] introduce the total conductance to be

$$G_{p/ap} = G_T(1 \pm P_1P_2) + G_{SI} \tag{6}$$

where G_T denotes a prefactor for direct elastic tunneling, P_1 and P_2 the effective tunneling electron spin polarizations of the two ferromagnetic electrodes and G_{SI} the spin independent conductance. From the measurements of G_p and G_{ap} (see Figure 40) we can obtain $\bar{G} = 1/2(G_p + G_{ap})$, the mean conductance which is independent of the strongly temperature dependent spin polarizations P_1 and P_2. G_T is indeed temperature dependent, but only marginally.[92] Therefore, the temperature dependence of G_T will be neglected in the following. G_{SI} as a function of T is governed by hopping via trapped states in the barrier and hence has a power law dependence on T:

$$G_{SI} = ST^{\gamma}$$

[91] C. Shang, J. Nowak, *et al.*, *Physical Review B*, vol. 58, no. 6, R2917–R2920, 1998.

[92] C. Shang, J. Nowak, *et al.*, *Physical Review B*, vol. 58, no. 6, R2917–R2920, 1998.

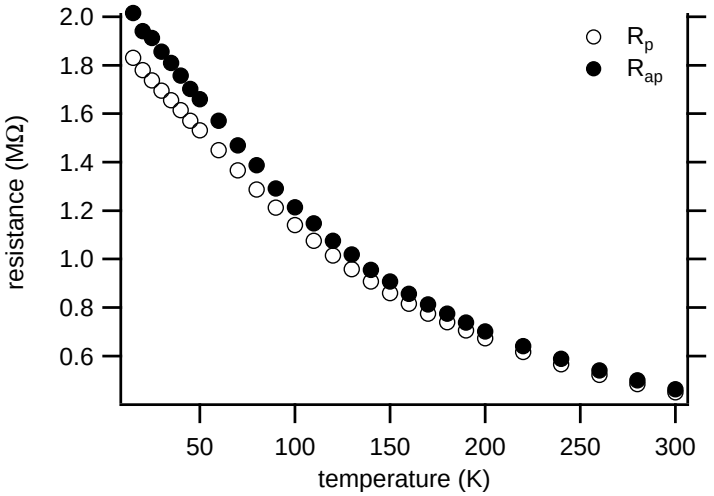

Figure 39: Temperature dependence of the resistance in the parallel (R_p) and antiparallel state (R_ap) for $Co_2FeSi/BaO(3.2\,nm)/Fe$ MTJs at $V_\mathrm{Bias} = 10\,\mathrm{mV}$.

where the constant S is dominated by the number of barrier defects.[93] According to theoretical work[94] the exponent γ depends on the number of path sections N the electrons travel through the barrier with $\gamma(N) = N - 2/(N+1)$. That means a direct path without hopping with $N = 1$ gives $\gamma = 0$ and the temperature dependence vanishes. Hopping through one trapped state gives $\gamma = 4/3$ and through two trapped states $\gamma = 5/2$. Fitting $\bar{G}$ to a power law dependence of the form $G_\mathrm{T} + ST^\gamma$ results in $\gamma = 1.423 \pm 0.006$ and $G_\mathrm{T} = (4.976 \pm 0.020) \times 10^{-7}\,\Omega^{-1}$ with the fit curve reproducing the data very well (see Figure 40). Considering the high uncertainty by totally neglecting the temperature dependence of G_T the γ obtained from the fit has a quite small mismatch with $\gamma = 1.33$ for $N = 2$. The discrepancy could originate from a small fraction of electrons hopping through two trapped states.

These findings are in good agreement with the strong bias dependence of the junctions which two-step tunneling can be held responsible for and also originates from defects in the barrier.

Åkerman et al.[95] apply Simmons[96] and Brinkman fits[97] on their temperature dependent I-V and $\mathrm{d}I/\mathrm{d}V$ curves respectively measured on MTJs with intact and shorted barrier which deliver the barrier height and barrier thickness as fit parameters. Although those parameters do not have any physical relevance[98] the findings of Åkerman et al. are nevertheless interesting. While

93 T. Hagler, R. Kinder, *et al.*, *Journal of Applied Physics*, vol. 89, no. 11, p. 7570, 2001.

94 L. Glazman and K. Matveev, *Sov. Phys. JETP*, vol. 67, no. June, pp. 1276–1282, 1988.

95 J. J. Åkerman, R Escudero, *et al.*, *Journal of Magnetism and Magnetic Materials*, vol. 240, pp. 86–91, 2002.

96 J. G. Simmons, *Journal of Applied Physics*, vol. 34, no. 9, pp. 2581–2590, 1963.

97 W. F. Brinkman, R. C. Dynes, *et al.*, *Journal of Applied Physics*, vol. 41, no. 5, pp. 1915–1921, 1970.

98 The employed models assume an amorphous barrier while the here used BaO and also MgO are crystalline.

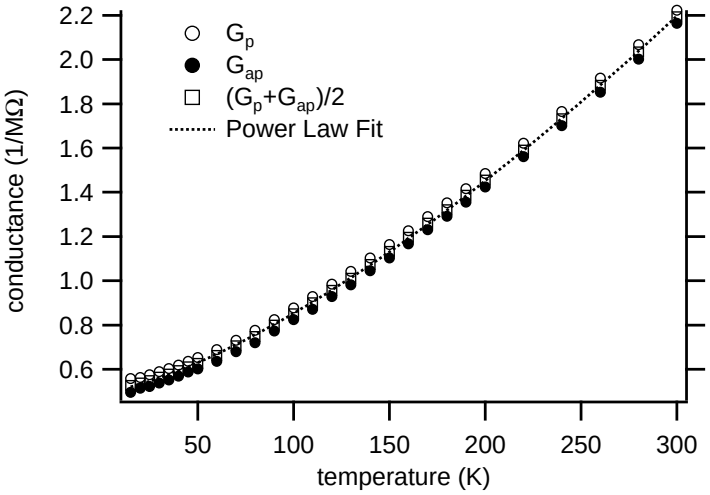

Figure 40: Conductance in the parallel state (G_p), antiparallel state (G_{ap}) and the mean conductance $\bar{G}$ as a function of the temperature and the fitting curve of $\bar{G}$ with a power law dependence.

the samples with an undamaged barrier show an increase of the barrier thickness and a decrease of the barrier height with rising temperatures, it is the reverse for the MTJs with shorted barrier. In Figure 41 the obtained fit parameters from Brinkman fits applied to the temperature dependent $\mathrm{d}I/\mathrm{d}V$ curves are plotted. In this process only the voltage range between $-150\,\mathrm{mV}$ and $+150\,\mathrm{mV}$ has been considered based on the methodology of Åkerman's group to gain comparable results. Our sample shows the same temperature dependence as the MTJs with shorted barrier which is another evidence for defects in the BaO layer leading to two or multi step tunneling.

In summary, we have succeeded in introducing BaO as a novel barrier material and in fabricating Co_2FeSi/BaO/Fe MTJs showing a TMR amplitude of up to 100 % at RT. Furthermore, a strong bias voltage dependence of the TMR in these MTJs has been observed which we hold two step tunneling responsible for due to defects within the BaO layer. This suspicion is substantiated by noise measurements indicating imperfections in the barrier. The obtained temperature dependence of the TMR could not be attributed to spin wave excitations, but from the fitted conductance as a function of temperature hopping through trapped states could be identified as origin and also the temperature dependent Brinkman fit parameters suggest a high defect rate in the barrier or at the interface.

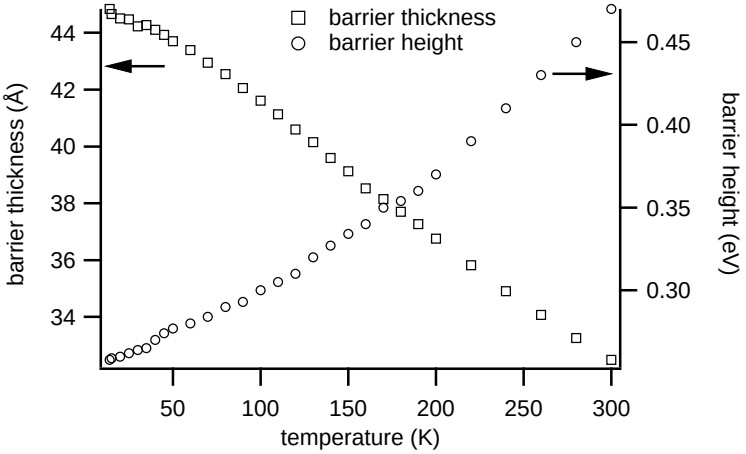

Figure 41: Barrier thickness (left axis) and height (right axis) obtained as fit parameters from the Brinkman fit plotted against the temperature.

Co_2FeAl based MTJs

Within our workgroup we have already successfully fabricated Co_2FeAl/MgO/CoFe MTJs with up to 147 % TMR ratio at RT,[99] so that an integration of Co_2FeAl into an MTJ with BaO barrier would not be connected with a time consuming optimization process of the lower electrode. On this account the Co_2FeAl layer is deposited – as shown by Ebke et al. – by magnetron sputtering. In this chapter the findings on Co_2FeAl based MTJs will be presented. Besides Co_2FeAl/BaO/Fe MTJs based on the Co_2FeSi/BaO/Fe design and described in section "Sample Preparation" on page 46 also an MgO/BaO double barrier has been studied. Here the idea has been to add a thin MgO layer between the lower electrode and the BaO barrier in order to increase the MTJs electric stability.

[99] D. Ebke, P. Thomas, *et al.*, *Journal of Magnetism and Magnetic Materials*, vol. 322, no. 8, pp. 996 –998, 2010.

Sample Preparation

The samples are prepared in a similar way as described in section "Sample Preparation" on page 46 starting with an MgO(001) substrate and a 5 nm thick MgO buffer layer. Then the 15 nm Co_2FeAl lower electrode is deposited by magnetron sputtering. Afterwards the sample is transferred into the MBE system and annealed at 500 °C for 10 minutes. Subsequently the BaO barrier layer is grown at $T_{sub} = 300\,°C$ by evaporating Ba metal in an O_2 atmosphere of 1×10^{-6} mbar. Then the Fe top electrode of 20 nm is deposited at the same substrate temperature. The samples are finalized by the sputter deposition of Ta(5 nm) / Au(50 nm) as capping layers.

Co_2FeAl/BaO/Fe MTJs

First, a sample basically prepared as described above[100] was investigated by means of Auger depth profiles. In an UHV

[100] The preparation has been done like outlined in the previous section with a BaO thickness of 2.8 nm. The only differences are reduced thicknesses of the capping layers with 2 nm Ta and 5 nm Au to reduce etching time in the subsequent Auger analysis.

environment a hole is milled into the sample surface by an ion beam while Auger electron spectra are taken. Because Auger electron spectroscopy is surface sensitive a precise depth profile of the materials contained in the layer stack is thereby obtained. Figure 42 shows the evaluated depth profile of the most relevant elements dependent on the etching time. The position of the electrodes (dark red curves) and Au capping (yellow) can clearly be identified. The top of the Fe electrode at ~15 minutes shows oxygen due to transportation time to the other deposition system which is used for the Ta/Au growth. The most outstanding feature is the Ba curve (green) from which one could conclude a diffusion of Ba into the Fe layer above and to a lesser extent into the subjacent Co_2FeAl electrode.

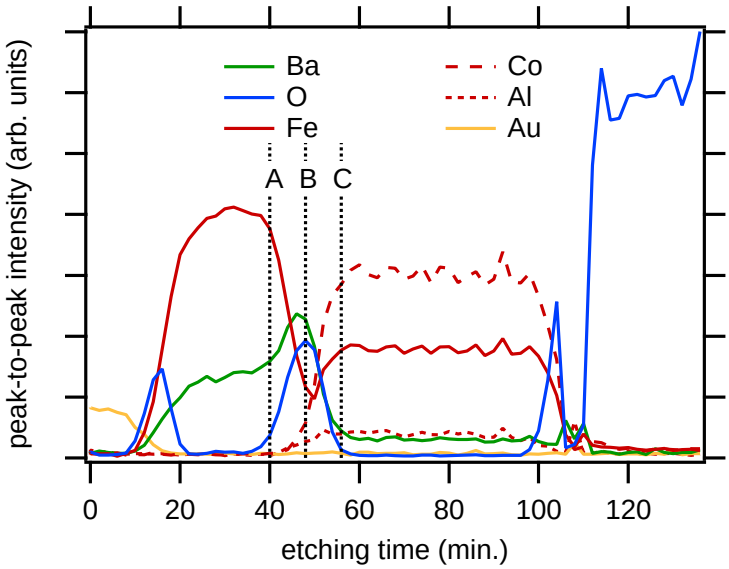

Figure 42: Element specific depth profile of a $Co_2FeAl/BaO/Fe$ MTJ obtained from Auger electron spectra. The vertical lines mark the positions at which the Auger electron spectra shown in Figure 43 were taken.

But looking at the Auger electron spectra (see Figure 43) right above the barrier layer (marked with "A"), within the barrier (marked with "B"), and below the barrier (marked with "C") and comparing them with the reference spectra of Fe and Ba it becomes clear, that a diffusion of Ba into the Fe layer cannot be proven. Curves A and C possess two minima between 585 eV and 600 eV which agree in their position and ratio with the Fe reference curve. Furthermore, the Fe characteristic minor minimum at $\sim$ 563 eV can clearly be identified. In contrast, the

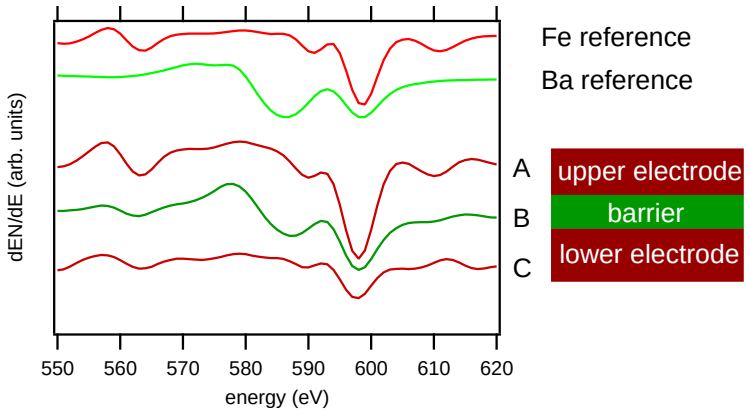

Figure 43: Characteristic detail of the Auger electron spectra of a Fe reference, a Ba reference, and a $Co_2FeAl/BaO/Fe$ sample. The curves A, B, and C were taken right above the barrier layer, within the barrier, and below the barrier respectively.

spectrum taken at a position in the middle of the barrier (curve B) the position of the minimum at 585 eV is slightly shifted to smaller energies compared to curves A and C and complies in its shape with the Ba reference. Thus a diffusion of Ba into either the Fe or the Co_2FeAl electrode is below the noise level of the measurement.

Transport measurements were carried out on a Co_2FeAl based MTJ with a thin BaO barrier of 2.8 nm ($(1 \times 0.3)\,\mu m^2$ MTJ with $RA \approx 400\,k\Omega\mu m^2$). From the I-V measurement an asymmetric conductance dI/dV (see Figure 44) with respect to the sign of the bias voltage and a dip structure at ± 105 mV marked by the vertical dashed lines are obtained. This feature could already be observed in $Co_2FeSi/BaO/Fe$ MTJs at ± 230 mV and as outlined there it confirms the crystallinity of our BaO barrier and implies that coherent tunneling is involved.[101] The same sample shows a negative TMR ratio of about $-10\,\%$ at RT (see Figure 45) with an applied bias voltage of $V_{\text{Bias}} = 10$ mV. According to Jullière's model a negative TMR ratio could be obtained if the electrodes' spin polarizations had the opposite signs like already reported on MTJs with a LSMO and a Fe_3O_4 electrode,[102] the latter having a negative spin polarization. But as this does not apply to our MTJs there must be another explanation for the negative TMR ratio. Tsymbal et al.[103] suggest that an impurity state in the barrier can exhibit a negative sign of the TMR ratio under certain conditions. If the energy E_i of the impurity state is near E_F and the tunneling electron's energy

[101] R. Matsumoto, S. Nishioka, *et al.*, *Solid State Communications*, vol. 143, pp. 574 –578, 2007; S. Tsunegi, Y. Sakuraba, *et al.*, *Applied Physics Letters*, vol. 93, no. 11, p. 112 506, 2008.

[102] G Hu and Y Suzuki, *Physical Review Letters*, vol. 89, no. 27, p. 276 601, 2002; G. Hu, R. Chopdekar, *et al.*, *Journal of Applied Physics*, vol. 93, p. 7516, 2003.

[103] E. Y. Tsymbal, A Sokolov, *et al.*, *Physical Review Letters*, vol. 90, no. 18, p. 186 602, 2003.

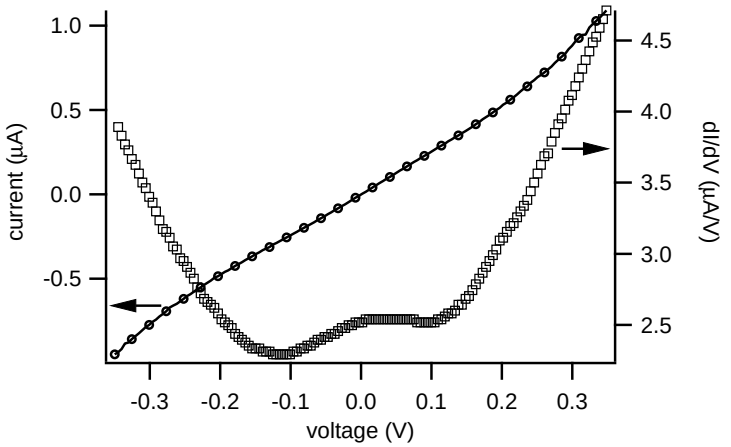

Figure 44: *I-V* and numerically deduced $\mathrm{d}I/\mathrm{d}V$ curve measured on a $(1 \times 0.3)\,\mu\mathrm{m}^2$ $Co_2FeAl/BaO(2.8\,\mathrm{nm})/Fe$ MTJ at RT.

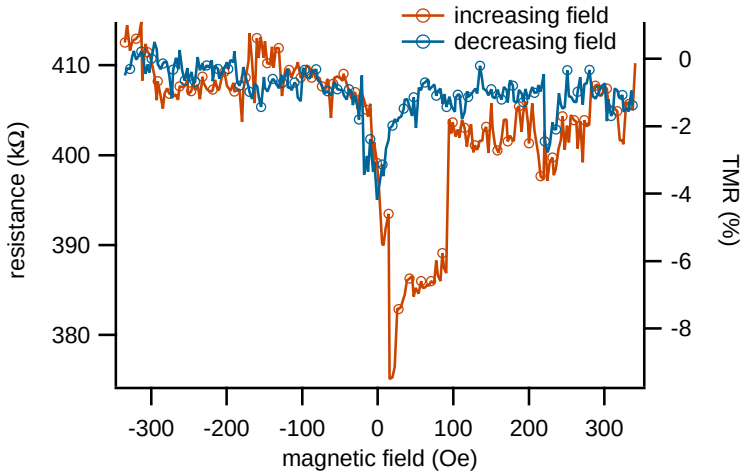

Figure 45: Major loop measured on a $(1 \times 0.3)\,\mu\mathrm{m}^2$ $Co_2FeAl/BaO(2.8\,\mathrm{nm})/Fe$ MTJ with $V_{\mathrm{Bias}} = 10\,\mathrm{mV}$ at RT.

is $E = E_i$ the spin conductance becomes inversely proportional to the DOS of one of the ferromagnetic electrodes resulting in a sign inversion of the TMR ratio. However, according to Tsymbal et al. this resonant tunneling can only dominate direct tunneling if the tunnel junction area is very small like their Ni/NiO/Co nanojunctions with areas $< 0.01\,\mu m^2$. This restriction on the junction area makes resonant tunneling as source of the negative TMR ratio in our MTJs appear to be quite unlikely and in addition limits the sign reversal to small bias voltages $|V| < \frac{E_i}{e}$. Heiliger et al.[104] have investigated the influence of interface structure on bias dependence of Fe/MgO/Fe MTJs by means of ab initio calculations in the framework of density functional theory with interesting results. They find a single layer of FeO between one electrode and the tunneling barrier to result in a negative TMR ratio over the whole investigated voltage range between $-1\,V$ and $+1\,V$. In the symmetrical case, i.e. an FeO layer on both sides of the barrier, the negative TMR region is restricted to a voltage range $> 0.5\,V$. The same approach for the same system by Zhang et al.[105] predicts negative TMR ratios for small voltages due to interface resonant states caused by the FeO interlayer.

[104] C. Heiliger, P. Zahn, *et al.*, *Physical Review B*, vol. 72, 180406(R), 2005.

[105] C Zhang, X.-G. Zhang, *et al.*, *Physical Review B*, vol. 69, p. 134 406, 2004.

From the XAS spectrum (see Figure 18) of the half junction Co_2FeAl/MgO it is proven that there are Fe oxides and – to a lesser extent – Co oxides in the Co_2FeAl/MgO interface region, so there could also be a thin interlayer of FeO (or less likely CoO) between the Co_2FeAl electrode and the BaO barrier which explains the obtained negative TMR ratio. A negative TMR could not be observed for Co_2FeSi based MTJs, which is probably due to the higher surface roughness of the Co_2FeSi surface and hence an inhomogeneous FeO interlayer which is not limited to one atomic layer. The XAS results presented in Figure 18 confirm this approach, as the indicators for Fe oxides are much more pronounced for Co_2FeSi than for Co_2FeAl.

$Co_2FeAl/MgO/BaO/Fe$ MTJs

The Co_2FeAl MTJs with an MgO/BaO double barrier are basically fabricated like described in section "Sample Preparation" on page 59. The only differences are a 0.8 nm MgO layer sputtered right after the Co_2FeAl layer and a reduction of the BaO layer thickness from 3 nm to 2.1 nm (see the schematic stack design in Figure 46). The *I-V* curve (see Figure 47) is highly un-

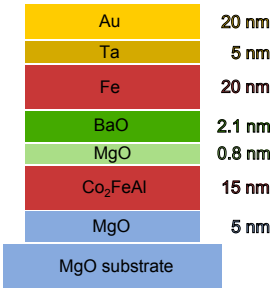

Figure 46: Schematic drawing of the fabricated Co_2FeAl based TMR layer stack with MgO/BaO double barrier.

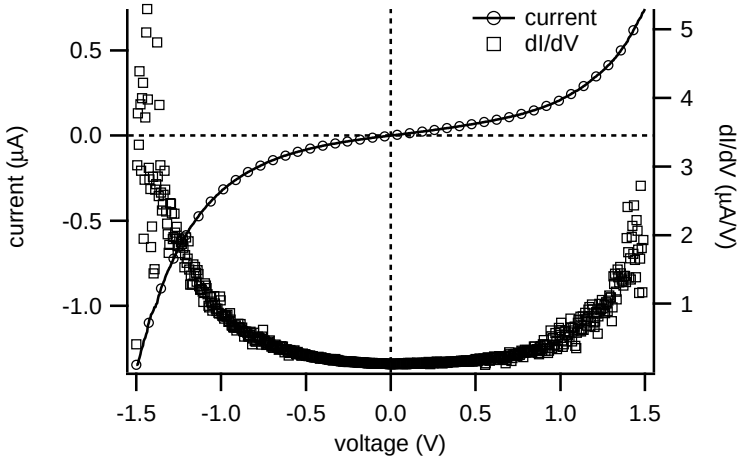

Figure 47: *I-V* (left axis) and $\mathrm{d}I/\mathrm{d}V$ curve (right axis) of a $(3 \times 1)\ \mu m^2$ MTJ with MgO/BaO double layer.

symmetric. The thin MgO interlayer effects the electric stability as all MTJs with a single barrier of BaO broke down when biased with comparable voltages. The MTJs show a moderately high TMR ratio of 29 % at $V_{Bias} = 10$ mV and 22 % at $V_{Bias} = 50$ mV (see Figure 48 obtained on a $(1 \times 0.3)\ \mu m^2$ MTJ with MgO/BaO double barrier).

The absolute resistances of the MTJs are very high with values between 1 MΩ ($(6 \times 2)\ \mu m^2$ MTJ) and 125 MΩ ($(0.6 \times 0.2)\ \mu m^2$ MTJ). This corresponds to an area resistance product of $RA = (48 \pm 8)\ M\Omega\mu m^2$. Since the TMR measurement setup is not equipped with an amplifier that makes it possible to measure the bias voltage dependence of the TMR ratio in a reasonable way – especially for very small bias voltages – it is not determined directly by measuring the major loops at small bias voltages but the *TMR-V* dependence is calculated from *I-V* curves measured in the parallel and anti-parallel state. As the anti-parallel state is only realized by the unequal switching behavior of the two magnetic electrodes and a slight dipole

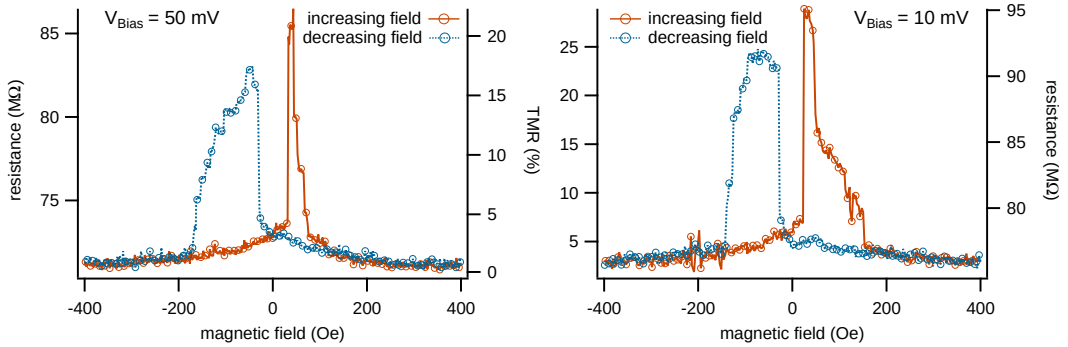

Figure 48: TMR measurement of a $(1 \times 0.3)\,\mu m^2$ MTJ with an MgO/BaO double barrier. Left: $V_{Bias} = 50\,mV$, right: $V_{Bias} = 10\,mV$.

coupling, the anti-parallel alignment of the electrodes' magnetizations is likely to be only partial. Hence, the assessed TMR ratios in Figure 49 are not the highest reachable values. That is in good agreement with the shown TMR measurements (see Figure 48) with the highest directly measured TMR ratio of 29 %. Nevertheless, the bias dependence becomes apparent from these findings and the shape of the shown curves reflects the usual bias dependence of MTJs with Heusler electrodes and MgO barrier[106] or other electrode and barrier materials,[107] but does not reproduce the strong bias dependence observed in Co_2FeSi/BaO/Fe MTJs.

Investigations on MTJs containing AlO_x/MgO double barriers[108] revealed a limitation of the observed TMR ratio by the highest obtainable TMR ratio with a single AlO_x barrier due to incoherent tunneling through the amorphous AlO_x layer. But here, the MgO/BaO double barrier delivers the highest TMR ratio at $V_{Bias} = 10\,mV$ among all investigated MTJs containing a BaO tunneling barrier which indicates a conservation of the coherent tunneling and a crystalline double barrier.

In summary, BaO could successfully be integrated into Co_2FeAl based MTJs with the lower Co_2FeAl electrode being deposited by DC magnetron sputtering. By means of Auger electron spectroscopy it could be proven that the applied temperatures during the BaO deposition and afterwards do not cause any diffusion of Ba neither into the lower Heusler compound electrode nor into the upper Fe electrode. A negative TMR ratio of -10 % was obtained for a Co_2FeAl/BaO(2.8 nm)/Fe MTJ which was explained by Fe oxides at the Co_2FeAl-BaO interface. The strong bias dependence as well as the temperature

[106] M Yamamoto, T Marukame, *et al.*, *Journal of Physics D: Applied Physics*, vol. 39, pp. 824–833, 2006.

[107] T. Zhu, X. Xiang, *et al.*, *Applied Physics Letters*, vol. 82, no. 16, p. 2676, 2003.

[108] O. Schebaum, V. Drewello, *et al.*, *Journal of Magnetism and Magnetic Materials*, vol. 323, no. 11, pp. 1525 –1528, 2011.

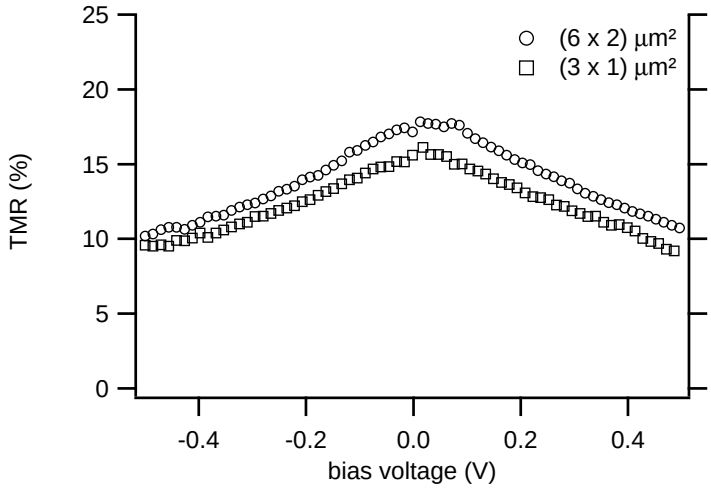

Figure 49: Bias voltage dependence of the TMR ratio of two $Co_2FeAl/MgO/BaO/Fe$ MTJs ($(6 \times 2)\ \mu m^2$ and $(3 \times 1)\ \mu m^2$) calculated from *I-V* curves measured in the parallel and anti-parallel state.

dependence of the TMR ratio could not be investigated due to a strong electric instability which causes breakdowns of the MTJs when measuring for a longer time or trying to bond them to a chip carrier required for low temperature measurements. This electric instability was even stronger than the one observed on $Co_2FeSi/BaO/Fe$ MTJs. By replacing the BaO tunneling barrier with an MgO/BaO double barrier the electric stability could effectively be increased at the expense of a very high resistance.

Conclusion and Outlook

In summary, Heusler compound thin films have successfully been grown from separate sources employing an MBE system recently established in our workgroup. In particular Co_2FeSi layers were deposited by means of two different techniques, namely co-evaporation and multilayer method. Both approaches yield B2 ordered thin films, however the latter procedure delivers smoother surfaces and a higher degree of B2 type Heusler ordering ($\sim 95\,\%$) which is why the multilayer method was chosen to fabricate the lower Co_2FeSi electrode of our MTJs. The crystallographic and magnetic properties are in good agreement and have been obtained from XRD analysis and AGM measurements respectively.

As the predicted half-metallicity of Co_2FeSi have not yet been experimentally proven using MgO tunneling barriers, BaO has been introduced as novel tunneling barrier in Co_2FeSi based MTJs due to the smaller lattice mismatch of BaO and Co_2FeSi compared to MgO and Co_2FeSi. XRD studies have shown that our partly custom made MBE system can be employed to produce thin BaO films with (001) ordered cubic crystal structure by evaporation of pure Ba metal in a low O_2 atmosphere. Here the substrate temperature and the O_2 pressure are the crucial factors, which have to be adjusted accurately, to really achieve BaO and not Ba, BaO_2, or mixed phases thereof.

The successful integration of BaO into Co_2FeSi/BaO/Fe MTJs with a maximum TMR ratio of more than 100 % at low bias voltages is the first reported study of BaO based MTJs in literature and can be seen as a great achievement. A strong bias dependence of the TMR ratio was observed which in this extent is not detected in MgO based MTJs. The steeply ascending TMR ratio with decreasing bias voltages could be attributed to two or multi step tunneling induced by defects in the barrier or the interface. Noise measurements strengthen this suspicion just as transport measurements at low temperatures do.

At high voltages the two step tunneling current dominates the direct tunneling current, while at very low voltages the two step tunneling current contribution becomes negligible and coherent tunneling prevails. This high TMR ratio at small V_{Bias} shows the large potential of a defect free BaO barrier.

As lower electrode also sputtered Co_2FeAl has been used, as it has been extensively studied within our workgroup. By means of an Auger depth profile on a Co_2FeAl/BaO/Fe MTJ a diffusion of BaO into either the Co_2FeAl or the Fe electrode could be excluded. The observed negative TMR ratio and dip structure in the $\mathrm{d}I/\mathrm{d}V$ curve on a MTJ with thinner BaO barrier layer is on the one hand caused by a thin FeO (or less likely CoO) at the Co_2FeAl/BaO interface which conforms with XAS investigations. On the other hand it shows the crystallinity of the barrier and the associated coherent tunneling process.

The problem of electric instability of the investigated Heusler based MTJs with pure BaO tunneling barrier could significantly be improved by inserting a thin MgO layer between the Co_2FeAl electrode and the BaO layer at the expense of a very high resistance.

Overall, important fundamental results could be obtained that provide a promising basis for further investigations on BaO based MTJs. Particularly for verifying the 100 % spin polarization predicted for many Heusler compounds eminent preliminary work has been provided. The boost in TMR ratio connected with it is not only interesting for pure research but also promising from the technological point of view.

Electron magnetic circular dichroism (EMCD)[109] investigations are currently carried out on selected Co_2FeAl and Co_2FeSi based TMR stacks at the Vienna University of Technology which promise to yield further information on the Heusler - BaO interface. More precisely EMCD allows to map the element specific magnetic moments on a transmission electron microscopy (TEM) lamella with the TEM typical high resolution.

[109] P. Schattschneider, S. Rubino, *et al.*, *Nature*, vol. 441, no. 7092, pp. 486–488, 2006.

The very next step is the construction of a measurement setup which is particularly designed to apply very small bias voltages with high accuracy to further study the bias dependence. Moreover the desired stronger amplification would be suitable for MgO/BaO double barriers or even MgO/BaO/MgO sandwich barriers with their expected high resistances.

By means of *inelastic electron tunneling spectroscopy (IETS)* measurements, one could further investigate the tunneling mechanism to e.g. prove or exclude if magnon excitations contribute

to the observed temperature dependence.[110]

As it has been shown that the demanded stoichiometry and crystal structure of BaO can only be achieved for a very small T_{sub} and p_{O_2} range, the BaO barrier should further be optimized particularly considering the verified barrier defects. A barrier optimization could also allow a reduction of the barrier layer thickness which would significantly reduce the MTJs' resistances and thus making it more suitable for applications. On the other hand, inducing oxygen vacancies in the BaO barrier in a controlled way could be exploited for memristive switching. It was shown[111] that oxygen vacancies in MgO based MTJs migrate within the MgO barrier due to the applied electric field and thereby reversibly change the MTJs resistance.

Because sputtered Co_2FeAl does not need high annealing temperatures for B2 type ordering it is perfectly suited as upper Heusler electrode for the fabrication of MTJs containing two Heusler electrodes. In combination with a pinning of the upper electrode promising findings could be achieved.

As small stoichiometric variations can have a great impact on the obtainable TMR ratio[112] we will investigate slight changes in composition of our Co_2FeSi electrode, at least in the interface region. In this regard the multilayer method offers the opportunity to easily adjust the termination layer towards the barrier layer and thereby e.g. reducing or even eliminating oxidation of the boundary layer. Among other properties this crucial interface feature should be investigated more extensively by XAS and XMCD studies.

The multilayer method can also be applied to other alloys and Heusler compounds. Co_2MnSi thin films could already be fabricated this way (see Figure 50), whereupon the individual layer thickness was doubled compared to the Co_2FeSi samples and the annealing was carried out ex-situ.

As spin polarized tunneling through an MgO barrier into a superconducting AlSi electrode did only yield a spin polarization $P = 55\,\%$ for Co_2FeAl,[113] replacing the MgO with BaO could be promising for both Co_2FeAl and Co_2FeSi as well as Co_2MnSi investigations.

Another very interesting aspect of BaO would be a barrier thickness dependence study of the TMR ratio. Yuasa et al.[114] have observed an oscillation of the TMR ratio with barrier thickness with a period of 0.30 nm for epitaxial Fe/MgO/Fe MTJs. The BaO barrier would potentially deliver a different oscillation period which could give deeper insights into the tunneling

[110] V. Drewello, "Tunneling spectroscopy of magnetic tunnel junctions", PhD thesis, Bielefeld University, 2010.

[111] P. Krzysteczko, "Memristive tunnel junctions", PhD thesis, Bielefeld University, 2010.

[112] M. Yamamoto, T. Ishikawa, *et al.*, *Journal of physics. Condensed matter: an Institute of Physics journal*, vol. 164212, 2010; H.-X. Liu, Y. Honda, *et al.*, *Applied Physics Letters*, vol. 101, no. 13, p. 132 418, 2012.

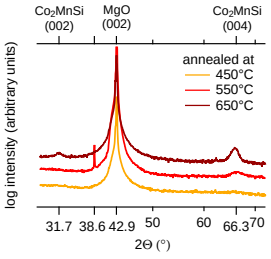

Figure 50: XRD spectra of 40 nm thick Co_2MnSi layers on MgO (001) substrate fabricated by MBE multilayer method and ex-situ annealed for 1 h.

[113] O. Schebaum, D. Ebke, *et al.*, *Journal of Applied Physics*, vol. 107, no. 9, pp. 09C717–09C717, 2010.

[114] S. Yuasa, T. Nagahama, *et al.*, *Nature Materials*, vol. 3, pp. 868–871, 2004.

mechanism.

An application – particularly promising from the technological point of view – is the use of BaO as barrier in Mn_3Ga based perpendicular MTJs (p-MTJs). With an in-plane lattice constant of $a_{Mn_3Ga} = 3.905\,\text{Å}$[115] the 45° rotated Mn_3Ga plane with $\sqrt{2} \cdot a_{Mn_3Ga} = 5.52\,\text{Å}$ is perfectly lattice matched to BaO ($a_{BaO} = 5.53\,\text{Å}$) and hence offers ideal conditions for fully epitaxial growth.

[115] J. Winterlik, B. Balke, *et al.*, *Phys. Rev. B*, vol. 77, p. 054 406, 2008.

Appendix

Custom made Knudsen cell

Figure 52 shows sketches of the Knudsen cell which was custom designed and constructed with the help of the physics department's mechanical workshop. It starts with the welding of the current feedthroughs, thermocouple feedthrough, and mountings for the heating wire construction into the CF40 flange. The latter can hold threaded rods on which the holding construction can be screwed. The tungsten heating wire is bent to form a meander and cylindrically rolled so that the Boron nitride (BN)[116] rings can be slipped over the heating wire cylinder. The wire strings are then laced into drill holes to avoid short cuts between the separate coils and stabilize the heating wire construction. A cylinder made of a Ta sheet is then put over the wire construction. After that additional four Ta cylinders are concentrically put over the first cylinder as a thermal shield. Between each of the four Ta cylinders is a Ta wire which is spirally coiled around the respective smaller one and secured by spot weldings. In this way the thermal contact between the Ta cylinders is reduced and the isolating effect of the shielding increased. In the next step the threaded rods are screwed into tapped holes in the lower side of the holding "pan" (see Figure 51) and the other sides of the rods inserted into the mountings in the flange. After that the heating wire construction is put on top of the holding "pan" and the Ta cylinders screwed on it laterally. Finally the heating wire has to be connected to the current feedthroughs and the twisted ends of thermocouple wires put into the correct position right underneath the point where the crucible will be arranged later.

In Figure 53 a side view of an earlier and slightly different version of the custom made Knudsen cell is shown. Compared to the above described version the mounting of the thermal shielding is not completely screwed but is held in place by Ta

[116] A high purity hexagonal Boron nitride ceramic was used which exhibits a high electric resistivity, thermal stability under vacuum up to 3000 °C, and low outgassing.

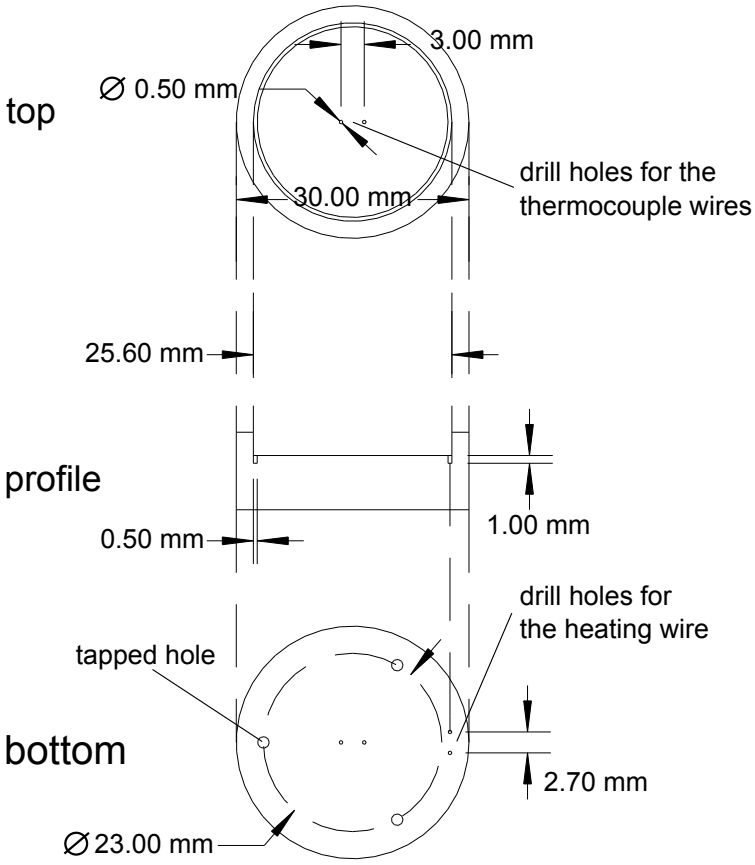

Figure 51: Sketch of the holding pan.

flaps screwed to the holding "pan". This construction can be seen in Figure 54 which also shows the heating wire connected to the current feedthroughs and the thermocouple wires welded to the respective contacts of the feedthrough. Figure 55 shows a view into the heating part of the Knudsen cell with the heating filament held in distance by the BN rings and surrounded by the Ta thermal shield. At the bottom the thermocouple can be identified.

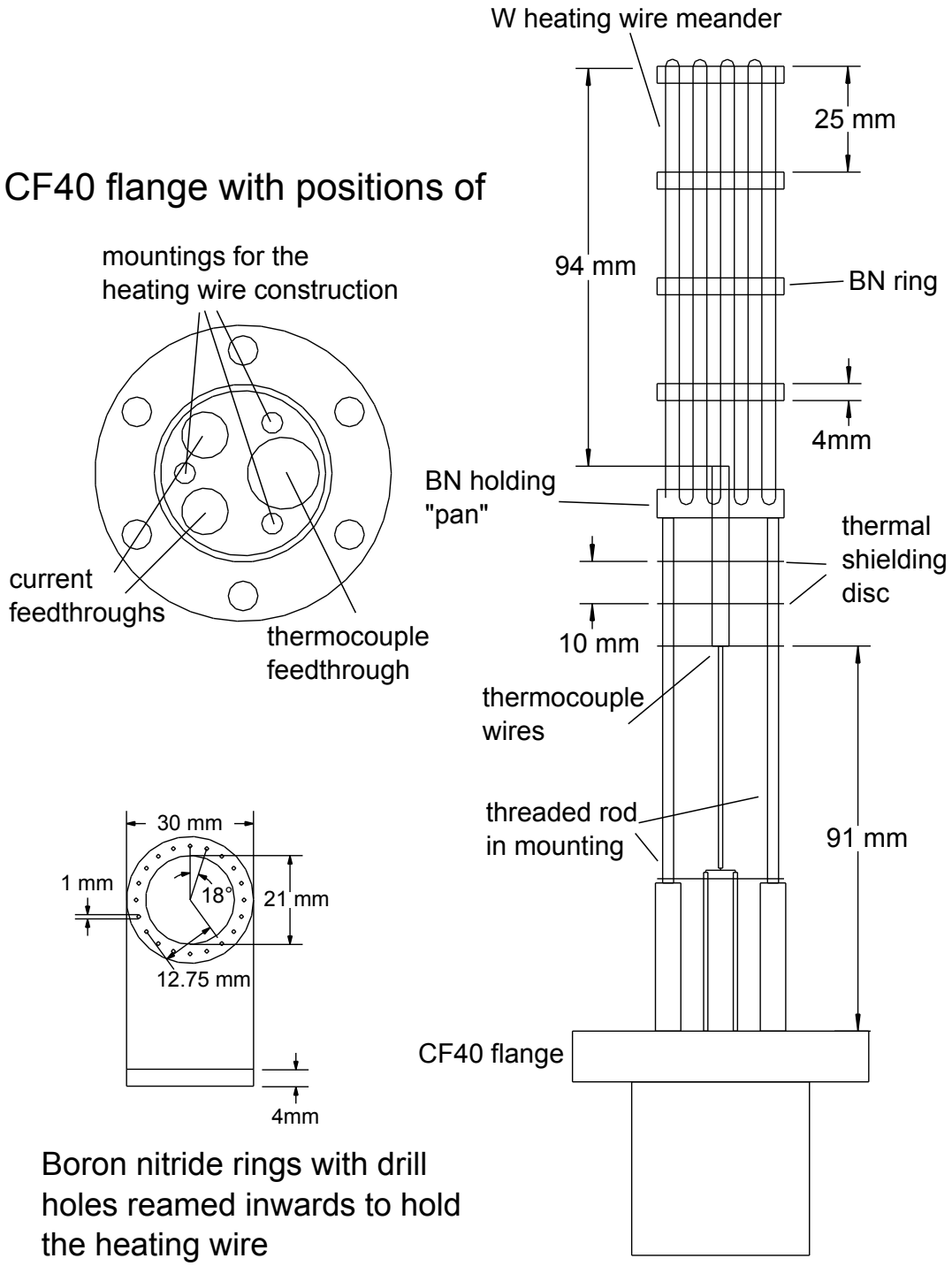

Figure 52: Sketch of the custom made Knudsen cell.

Figure 53: Side view of an older, slightly different version of the custom made Knudsen cell. The mounting of the thermal shielding is not completely screwed but is held in place by Ta flaps screwed to the holding "pan". Furthermore the threaded rods of the final version are stronger.

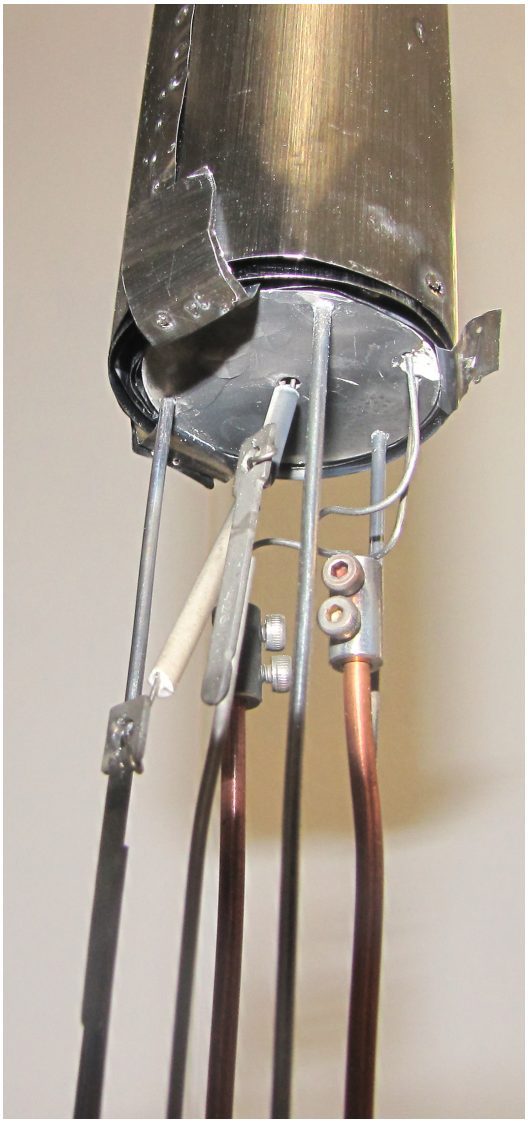

Figure 54: Detailed view onto the lower side of the holding pan with heating wire connections and thermocouple wires welded to the feedthrough contacts.

Figure 55: Topview into the heating part of the Knudsen cell which encloses the crucible.

Bibliography

[Agm] *Princeton measurement corporation - micromag 2900 agm magnetometer instruction manual*, 2004.

[AM+00] H. Akinaga, T. Manago, and M. Shirai, *Japanese Journal of Applied Physics*, vol. 39, p. 1118, 2000.

[AR+03] J. Akerman, I. Roshchin, J. Slaughter, R. Dave, and I. Schuller, *EPL (Europhysics)*, vol. 63, no. 1, pp. 104–110, 2003.

[BB+88] M. N. Baibich, J. M. Broto, A. Fert, F. Nguyen van Dau, F. Petroff, P. Etienne, G. Creuzet, A. Friederich, and J. Chazelas, *Physical Review Letters*, vol. 61, pp. 2472–2475, 1988.

[BC+04] T. Block, M. Carey, B. Gurney, and O. Jepsen, *Physical Review B*, vol. 70, no. 20, pp. 1–5, 2004.

[BD+70] W. F. Brinkman, R. C. Dynes, and J. M. Rowell, *Journal of Applied Physics*, vol. 41, no. 5, pp. 1915–1921, 1970.

[BE+11] P. Bruski, S. Erwin, M. Ramsteiner, O. Brandt, K.-J. Friedland, R. Farshchi, J. Herfort, and H. Riechert, *Physical Review B*, vol. 83, no. 14, pp. 2–5, 2011.

[BF+06] B. Balke, G. H. Fecher, H. C. Kandpal, C. Felser, K. Kobayashi, E. Ikenaga, J.-J. Kim, and S. Ueda, *Phys. Rev. B*, vol. 74, p. 104 405, 2006.

[BF+90] J. Barnaś, A. Fuss, R. E. Camley, P. Grünberg, and W. Zinn, *Phys. Rev. B*, vol. 42, pp. 8110–8120, 13 1990.

[BZ+01] W. H. Butler, X.-G. Zhang, T. C. Schulthess, and J. M. MacLaren, *Phys. Rev. B*, vol. 63, p. 054 416, 2001.

[CB+04] M. J. Carey, T. Block, and B. A. Gurney, *Applied Physics Letters*, vol. 85, no. 19, pp. 4442–4444, 2004.

[CI+95] C. Chen, Y. Idzerda, H.-J. Lin, N. Smith, G Meigs, E Chaban, G. Ho, E Pellegrin, and F Sette, *Physical Review Letters*, vol. 75, no. 1, pp. 152–155, 1995.

[CS01] B. Cullity and S. Stock, *Elements of X-ray Diffraction*. Prentice hall Upper Saddle River, NJ, 2001, vol. 3.

[DR+02] Y. S. Dedkov, U. Rüdiger, and G. Güntherodt, *Phys. Rev. B*, vol. 65, p. 064 417, 6 2002.

[Dre10] V. Drewello, "Tunneling spectroscopy of magnetic tunnel junctions", PhD thesis, Bielefeld University, 2010.

[DTFP+07] J. De Teresa, A. Fernández-Pacheco, L. Morellon, J. Orna, J. Pardo, D. Serrate, P. Algarabel, and M. Ibarra, *Microelectronic engineering*, vol. 84, no. 5, pp. 1660–1664, 2007.

[Ebk10] D. Ebke, "Cobalt based Heusler compounds in magnetic tunnel junctions", PhD thesis, Bielefeld University, 2010.

[ET+10] D. Ebke, P. Thomas, O. Schebaum, M. Schäfers, D. Nissen, V. Drewello, A. Hütten, and A. Thomas, *Journal of Magnetism and Magnetic Materials*, vol. 322, no. 8, pp. 996 –998, 2010.

[FF07] G. H. Fecher and C. Felser, *Journal of Physics D: Applied Physics*, vol. 40, no. 6, p. 1582, 2007.

[Gal05] I Galanakis, *Physical Review B*, vol. 71, p. 012 413, 2005.

[GD+02] I. Galanakis, P. Dederichs, and N. Papanikolaou, *Physical Review B*, vol. 66, no. 17, pp. 1–9, 2002.

[GH+08] O. Gaier, J. Hamrle, S. J. Hermsdoerfer, H. Schultheiß, B. Hillebrands, Y. Sakuraba, M. Oogane, and Y. Ando, *Journal of Applied Physics*, vol. 103, p. 103 910, 2008.

[GM+83] R. A. de Groot, F. M. Mueller, P. G. v. Engen, and K. H. J. Buschow, *Phys. Rev. Lett.*, vol. 50, pp. 2024–2027, 25 1983.

[GM88] L. Glazman and K. Matveev, *Sov. Phys. JETP*, vol. 67, no. June, pp. 1276–1282, 1988.

[HC+03] G. Hu, R. Chopdekar, and Y Suzuki, *Journal of Applied Physics*, vol. 93, p. 7516, 2003.

[HK+01] T. Hagler, R. Kinder, and G. Bayreuther, *Journal of Applied Physics*, vol. 89, no. 11, p. 7570, 2001.

[HS+03] F. Heusler, W. Starck, and E. Haupt, *Verhandlungen der deutschen physikalischen Gesellschaft*, vol. Bd. 5, D. P. G. (1899-1945), Ed., pp. 219–232, 1903.

[HS02] G Hu and Y Suzuki, *Physical Review Letters*, vol. 89, no. 27, p. 276 601, 2002.

[HZ+05] C. Heiliger, P. Zahn, B. Y. Yavorsky, and I. Mertig, *Physical Review B*, vol. 72, 180406(R), 2005.

[IH+08] S. Ikeda, J. Hayakawa, Y. Ashizawa, Y. M. Lee, K. Miura, H. Hasegawa, M. Tsunoda, F. Matsukura, and H. Ohno, *Applied Physics Letters*, vol. 93, no. 8, p. 082 508, 2008.

[IM+06] T. Ishikawa, T. Marukame, K.-i. Matsuda, T. Uemura, M. Arita, and M. Yamamoto, *Journal of Applied Physics*, vol. 99, 08J110, 2006.

[JA+92] T. Jondo, R. Abraham, M. Cohen-Adad, and J. Jorda, *Journal of alloys and compounds*, vol. 186, no. 2, pp. 347–359, 1992.

[Jul75] M. Jullière, *Physics Letters A*, vol. 54, pp. 225–226, 1975.

[Krz10] P. Krzysteczko, "Memristive tunnel junctions", PhD thesis, Bielefeld University, 2010.

[KS+07] M Kallmayer, H Schneider, G Jakob, H. J. Elmers, B Balke, and S Cramm, *Journal of Physics D: Applied Physics*, vol. 40, pp. 1552–1557, 2007.

[LC+06] T. Lv, D. Chen, and M. Huang, *Journal of Applied Physics*, vol. 100, p. 086 103, 2006.

[LH+12] H.-X. Liu, Y. Honda, T. Taira, K. ichi Matsuda, M. Arita, T. Uemura, and M. Yamamoto, *Applied Physics Letters*, vol. 101, no. 13, p. 132 418, 2012.

[LL+11] Z. Q. Lei, G. J. Li, W. F. Egelhoff, P. T. Lai, and P. W. T. Pong, *IEEE Transactions on Magnetics*, vol. 47, no. 3, pp. 602–612, 2011.

[LM+91] S. H. Liou, S Malhotra, Z. S. Shan, D. J. Sellmyer, S Nafis, J. Woolam, C. Reed, R. DeAngelis, and G. Chow, *Journal of Applied Physics*, vol. 70, p. 5882, 1991.

[MC+06] G.-X. Miao, K. B. Chetry, A. Gupta, W. H. Butler, K. Tsunekawa, D. Djayaprawira, and G. Xiao, *Journal of Applied Physics*, vol. 99, no. 8, 08T305, 2006.

[MJ+98] A. MacDonald, T. Jungwirth, and M. Kasner, *Physical Review Letters*, vol. 81, no. 3, pp. 705–708, 1998.

[MK+95] J. S. Moodera, L. R. Kinder, T. M. Wong, and R. Meservey, *Phys. Rev. Lett.*, vol. 74, no. 16, pp. 3273–3276, 1995.

[MN+07] R. Matsumoto, S. Nishioka, M. Mizuguchi, M. Shiraishi, H. Maehara, K. Tsunekawa, D. D. Djayaprawira, N. Watanabe, Y. Otani, T. Nagahama, A. Fukushima, H. Kubota, S. Yuasa, and Y. Suzuki, *Solid State Communications*, vol. 143, pp. 574 –578, 2007.

[MP60] R. Meyer and E. Pietsch, *Gmelins Handbuch der anorganischen Chemie: Barium Ergänzungsband*, 30. Verlag Chemie, 1960.

[MT94] R. Meservey and P. Tedrow, *Physics Reports*, vol. 238, no. 4, pp. 173 –243, 1994.

[MT95] T. Miyazaki and N. Tezuka, *Journal of Magnetism and Magnetic Materials*, vol. 139, pp. L231–L234, 1995.

[NN+11] M. Nobori, T. Nakano, J. Hasegawa, G. Oomi, Y. Sakuraba, K. Takanashi, Y. Miura, Y. Ohdaira, and Y. Ando, *Physical Review B*, vol. 83, no. 10, pp. 1–6, 2011.

[NS99] J. Nogués and I. K. Schuller, *Journal of Magnetism and Magnetic Materials*, vol. 192, pp. 203–232, 1999.

[OY+07] M. Oogane, R. Yilgin, M. Shinano, S. Yakata, Y. Sakuraba, M. Oogane, R. Yilgin, M. Shinano, S. Yakata, and Y. Sakuraba, *Journal of Applied Physics*, vol. 101, 09J501, 2007.

[OY+97] T. Ohnishi, M. Yoshimoto, G. H. Lee, T. Maeda, and H. Koinuma, *Journal of Vacuum Science & Technology A: Vacuum, Surfaces, and Films*, vol. 15, no. 5, pp. 2469–2472, 1997.

[PA+08] P. V. Paluskar, J. J. Attema, G. A. de Wijs, S. Fiddy, E. Snoeck, J. T. Kohlhepp, H. J. M. Swagten, R. A. de Groot, and B. Koopmans, *Phys. Rev. Lett.*, vol. 100, p. 057 205, 2008.

[Pri98] G. A. Prinz, *Science*, vol. 282, no. 5394, pp. 1660–1663, 1998.

[PV+98] J.-H. Park, E. Vescovo, H.-J. Kim, C. Kwon, R. Ramesh, and T. Venkatesan, *Nature*, vol. 392, no. 6678, pp. 794–796, 1998.

[RO+01] T. Regan, H Ohldag, C Stamm, F Nolting, J Lüning, J Stöhr, and R. White, *Physical Review B*, vol. 64, p. 214 422, 2001.

[Rog08] J. Rogge, "Untersuchungen an vollständig thermisch gedampften Fe/MgO/Fe Tunnelelementen und NaCl Schichten", Diplomarbeit, Bielefeld University, 2008.

[Sch18] P. Scherrer, *Göttinger Nachrichten*, 1918.

[Sch86] K Schwarz, *Journal of Physics F: Metal Physics*, vol. 16, no. 9, p. L211, 1986.

[SD+11] O. Schebaum, V. Drewello, A. Auge, G. Reiss, M. Münzenberg, H. Schuhmann, M. Seibt, and A. Thomas, *Journal of Magnetism and Magnetic Materials*, vol. 323, no. 11, pp. 1525 –1528, 2011.

[SE+10] O. Schebaum, D. Ebke, A. Niemeyer, G. Reiss, J. Moodera, and A. Thomas, *Journal of Applied Physics*, vol. 107, no. 9, pp. 09C717–09C717, 2010.

[SH59] G. Saum and E. Hensley, *Physical Review*, vol. 113, no. 4, pp. 1019–1022, 1959.

[Sim63] J. G. Simmons, *Journal of Applied Physics*, vol. 34, no. 9, pp. 2581–2590, 1963.

[SK+04] J Schmalhorst, S Kämmerer, M Sacher, G Reiss, A Hütten, and A Scholl, *Physical Review B*, vol. 70, p. 024 426, 2004.

[SM10] F. Schmid-Michels, "Herstellung und Charakterisierung von Co_2FeMg", Bachelor's Thesis, Bielefeld University, 2010.

[SN+98] C. Shang, J. Nowak, R. Jansen, and J. Moodera, *Physical Review B*, vol. 58, no. 6, R2917–R2920, 1998.

[SR+06] P. Schattschneider, S. Rubino, C. Hebert, J. Rusz, J. Kunes, P. Novak, E. Carlino, M. Fabrizioli, G. Panaccione, and G. Rossi, *Nature*, vol. 441, no. 7092, pp. 486–488, 2006.

[Ste77] M. B. Stearns, *Journal of Magnetism and Magnetic Materials*, vol. 5, pp. 167–171, 1977.

[TB+02] E. Tsymbal, V. Burlakov, and I. Oleinik, *Physical Review B*, vol. 66, no. 7, pp. 3–6, 2002.

[TI+09] N. Tezuka, N. Ikeda, F. Mitsuhashi, and S. Sugimoto, *Applied Physics Letters*, vol. 94, no. 16, p. 162 504, 2009.

[TM73] P. Tedrow and R Meservey, *Physical Review B*, vol. 7, no. 1, pp. 318–326, 1973.

[TN+09] Y. Takamura, R. Nakane, and S. Sugahara, *Journal of Applied Physics*, vol. 105, no. 7, 07B109, 2009.

[TS+03] E. Y. Tsymbal, A Sokolov, I. F. Sabirianov, B Doudin, and G. P. G. Ap, *Physical Review Letters*, vol. 90, no. 18, p. 186 602, 2003.

[TS+08] S. Tsunegi, Y. Sakuraba, M. Oogane, K. Takanashi, and Y. Ando, *Applied Physics Letters*, vol. 93, no. 11, p. 112 506, 2008.

[VB+01] A Vedyayev, D Bagrets, A Bagrets, and B Dieny, *Physical Review B*, vol. 63, no. 6, p. 064 429, 2001.

[WA+01] S. A. Wolf, D. D. Awschalom, R. A. Buhrman, J. M. Daughton, S. von MolnÃąr, M. L. Roukes, A. Y. Chtchelkanova, and D. M. Treger, *Science*, vol. 294, no. 5546, pp. 1488–1495, 2001.

[WB+08] J. Winterlik, B. Balke, G. H. Fecher, C. Felser, M. C. M. Alves, F. Bernardi, and J. Morais, *Phys. Rev. B*, vol. 77, p. 054 406, 2008.

[Web71] P. Webster, *Journal of Physics and Chemistry of Solids*, vol. 32, no. 6, pp. 1221 –1231, 1971.

[WF+05] S. Wurmehl, G. Fecher, H. Kandpal, V. Ksenofontov, C. Felser, H.-J. Lin, and J. Morais, *Physical Review B*, vol. 72, no. 18, pp. 1–9, 2005.

[WF+06] S. Wurmehl, G. H. Fecher, H. C. Kandpal, V. Ksenofontov, C. Felser, and H.-J. Lin, *Applied Physics Letters*, vol. 88, no. 3, p. 032 503, 2006.

[WH53] G. Williamson and W. Hall, *Acta Metallurgica*, vol. 1, no. 1, pp. 22–31, 1953.

[YI+10] M. Yamamoto, T. Ishikawa, and T. Taira, *Journal of physics. Condensed matter: an Institute of Physics journal*, vol. 164212, 2010.

[YM+06] M Yamamoto, T Marukame, T Ishikawa, K Matsuda, T Uemura, and M Arita, *Journal of Physics D: Applied Physics*, vol. 39, pp. 824–833, 2006.

[YN+04] S. Yuasa, T. Nagahama, A. Fukushima, Y. Suzuki, and K. Ando, *Nature Materials*, vol. 3, pp. 868–871, 2004.

[YY+12] H. Yang, S.-H. Yang, and S. Parkin, *AIP Advances*, vol. 2, no. 1, p. 012 150, 2012.

[YY11] H. L. Yu and G. W. Yang, *Applied Physics Letters*, vol. 98, no. 1, p. 011 910, 2011.

[ZL+97] S. Zhang, P. Levy, a. Marley, and S. Parkin, *Physical Review Letters*, vol. 79, no. 19, pp. 3744–3747, 1997.

[Zol58] R. Zollweg, *Physical Review*, vol. 111, no. 1, pp. 113–119, 1958.

[ZS20] R. Zsigmondy and P. Scherrer, *Kolloidchemie: ein Lehrbuch*, ser. Chemische Technologie in Einzeldarstellungen. O. Spamer, 1920.

[ZW98] J. Zhang and R. M. White, *Journal of Applied Physics*, vol. 83, no. 11, p. 6512, 1998.

[ZX+03] T. Zhu, X. Xiang, and J. Q. Xiao, *Applied Physics Letters*, vol. 82, no. 16, p. 2676, 2003.

[ZZ+04] C Zhang, X.-G. Zhang, P. Krstic, H Cheng, W. Butler, and J. Maclaren, *Physical Review B*, vol. 69, p. 134 406, 2004.

[ÅE+02] J. J. Åkerman, R Escudero, C Leighton, S Kim, D. A. Rabson, R. Whig, J. M. Slaughter, and I. K. Schuller, *Journal of Magnetism and Magnetic Materials*, vol. 240, pp. 86–91, 2002.

Acknowledgment

At this point I would like express my gratitude to all people that have supported me in completing this work. First, it is my most pleasent duty to thank my supervisor *Prof. Dr. Andreas Hütten* for giving me the opportunity to research this challenging topic and always being optimistic despite all problems and throwbacks during the last about three years.

Moreover I would like to give thanks to *Prof. Dr. Günther Reiss* for the chance of using his laboratories and *Dr. Andy Thomas* for providing me with his LaTeX style.

Actually, I want to say thank you to all members of D2, but I have to point out a few colleagues who have been exceedingly helpful. I thank *Fabian Schmid-Michels* for the programming of the control software and his great support with the planning and construction of the custom made Knudsen cells. I am obligated to *Peter Hedwig* for carrying out the noise measurements and supporting me with the typographic corrections of this work, *Alex Böhnke* for the AFM measurements and *Christian Sterwerf* for providing me with the Co_2FeSi/MgO/CoFe reference samples. Furthermore I am grateful for the XAS and XMCD as well as AGM measurements by *Manuel Glas* and the preparation of the Ba pieces by *Nadine Mill*. I also thank *Dr. Jan Schmalhorst* for the Auger depth profile, *Markus Schäfers* for the long hours he spent for bonding (tries) and *Aggi Windmann* for her support concerning the administrative peculiarities.

Special thanks are due to *Dr. Karsten Rott* for his instructions in vacuum technology, e^--beam lithography and virtually all laboratory knowledge. I also thank *Savio Fabretti* for the many fruitful discussions and distractions whenever they have been required and *Dr. Daniel Ebke* for helpful talks and suggestions. I may not forget to say thank you to my office co-inhabitants not mentioned before *Stefan Niehörster* and *Daniel Meier* for the laid-back and pleasant office atmosphere.

I am very grateful for the financial support of my work by

the *Deutsche Forschungsgemeinschaft (DFG)* and the *Japan Science and Technology Agency (JST)* in the framework of an international collaboration.

In the end, I would like to apologize to all who I might have unintentionally forgotten to express my gratitude to and say a special thank you to my wife *Dinah* who has been supporting me over the whole time of my work and beyond.